Lawrence Berkeley National Laboratory
Recent Work

Title
PHASE TRANSITIONS AND MODULATED STRUCTURES IN ORDERED (Cu-Mn)3Al ALLOYS

Permalink
https://escholarship.org/uc/item/85s9z9hg

Authors
Bouchard, M.
Thomas, G.

Publication Date
1975-05-01

eScholarship.org
Powered by the California Digital Library
University of California

0 0 0 0 4 3 0 2 4 2 3

Submitted to Acta Metallurgica

RECEIVED
LAWRENCE
BERKELEY LABORATORY

AUG 29 1975

LIBRARY AND
DOCUMENTS SECTION

LBL-3719
Preprint c.1

PHASE TRANSITIONS AND MODULATED STRUCTURES IN ORDERED $(Cu\text{-}Mn)_3Al$ ALLOYS

M. Bouchard and G. Thomas

May 1975

Prepared for the U. S. Energy Research and
Development Administration under Contract W-7405-ENG-48

For Reference

Not to be taken from this room

LAWRENCE BERKELEY LABORATORY
UNIVERSITY OF CALIFORNIA
BERKELEY

LBL-3719
c.1

DISCLAIMER

This document was prepared as an account of work sponsored by the United States Government. While this document is believed to contain correct information, neither the United States Government nor any agency thereof, nor the Regents of the University of California, nor any of their employees, makes any warranty, express or implied, or assumes any legal responsibility for the accuracy, completeness, or usefulness of any information, apparatus, product, or process disclosed, or represents that its use would not infringe privately owned rights. Reference herein to any specific commercial product, process, or service by its trade name, trademark, manufacturer, or otherwise, does not necessarily constitute or imply its endorsement, recommendation, or favoring by the United States Government or any agency thereof, or the Regents of the University of California. The views and opinions of authors expressed herein do not necessarily state or reflect those of the United States Government or any agency thereof or the Regents of the University of California.

PHASE TRANSITIONS AND MODULATED STRUCTURES IN ORDERED $(Cu-Mn)_3Al$ ALLOYS

M. Bouchard* and G. Thomas

Department of Materials Science and Engineering, College of Engineering,
and Inorganic Materials Research Division, Lawrence Berkeley Laboratory,
University of California, Berkeley, California 94720

ABSTRACT

Quenched and aged alloys along the composition line Cu_3Al-Cu_2MnAl have been studied by electron diffraction and microscopy. Quenching produces an ordered solid solution based on the DO_3 structure of Cu_3Al and the $L2_1$ structure of Cu_2MnAl.

Below 350°C the alloys decompose inside a miscibility gap into a Cu_2MnAl-rich phase and a Cu_3Al-rich phase. The resulting microstructures possess all the metallographic characteristics of spinodal decomposition. The early stage of the decomposition is characterized by composition modulations having a range of wavevectors close to <100>. The wavelength developes into resolvable values of 40-100Å and gradually increases with aging time.

During coarsening, the symmetrical alloy developes a complex microstructure of <100> oriented rods having widely different wavelengths, whereas the Mn-rich asymmetrical alloys develop {100} oriented Cu_3Al-rich plates. On coarsening the coherency strain (~2%) is generally relieved by the generation of $\frac{1}{2}a<100>$ interfacial dislocations. Prior to the loss of coherency in the symmetrical alloy, the Cu_3Al-rich phase possesses a tetragonal structure whereas the Cu_2MnAl-rich phase has a cubic structure. After the loss of coherency, both phases are cubic.

---

* Present Address: Communication Research Center, P.O. Box 490, Station A, Ottawa, Canada

In the Al-rich asymmetrical alloy, the Cu_2MnAl-rich phase heterogenously nucleates at $\frac{1}{4}a\langle 111\rangle$ APB's.

In the symmetrical alloy, the structure of the Cu_3Al-rich particles varies with the decomposition temperature. At temperatures close to the miscibility gap, the structure of the particles is DO_3. These DO_3 particles are further modulated by a dense array of small regions having the $L1_0$ superstructure and exhibit tweed strain contrast. At lower temperatures, the particles are composed of a regular arrangement of twelve possible variants of the $L1_0$ phase. At all temperatures, the structure of the Cu_2MnAl-rich phase is $L2_1$.

During overaging of the symmetrical alloy at temperatures close to the miscibility gap, the Cu_3Al-rich phase transforms to the γ phase having a composition near Cu_9Al_4. Thus it is suggested that for the symmetrical alloy the decomposition tie line is close to Cu_9Al_4 - $Cu_{2.2}MnAl_{0.8}$.

I. INTRODUCTION

The metallography of the Cu-rich portion of the Cu-Mn-Al system has been fully investigated by West and Thomas(1) at temperatures above 450°C. They found that the addition of Mn expands the high temperature β phase field of the Cu-Al system. The compositional range of stability of the β phase increases with temperature, and includes the composition of the well known Heusler alloy Cu_2MnAl at temperatures above 650°C. At 400°C, the equilibrium phases in this alloy are: Cu_3Mn_2Al, γ and β_{Mn}. The precipitation of these phases can be suppressed by quenching (1-6). The high temperature β phase has a disordered bcc structure which orders rapidly during quenching. The ordering takes place in two stages(4,5,6), forming first the B2 structure at T_cB2 (750-770°C for Cu_2MnAl) and the $L2_1$ structure at T_cL2_1 (615°C for Cu_2MnAl).

The low temperature aging characteristics of the ternary alloys are strongly influenced by their compositions. In the stoichiometric alloy, Cu_2MnAl, the quenched ordered $L2_1$ structure is stable below 325°C(2,7). In non-stoichiometric alloys, the precipitation of other phases has been reported(2,7,8,9,10).

The alloys along the composition line Cu_3Al - Cu_2MnAl are of particular interest since the $L2_1$ structure of the Cu_2MnAl alloy resembles very closely the DO_3 structure of the binary Cu_3Al alloy, and the difference between their lattice parameters is only about 2% (a = 5.95Å and 5.83Å respectively)(8,10,11). Persson(10) using x-ray analysis discovered that aging of the $(Cu\text{-}Mn)_3Al$ alloys resulted in the separation of two cubic phases that could be interpreted as Cu_3Al and Cu_2MnAl. Johnston and Hall(2) also using an alloy near $Cu_{2.5}Mn_{0.5}Al$ (half way between Cu_3Al and Cu_2MnAl) showed the presence of side-bands after brief aging at 200°C and a double cubic structure after prolonged aging at 300°C. The aim of the present research was to study in more detail the structure and morphologies of alloys along the composition line Cu_3Al-Cu_2MnAl using electron diffraction and microscopy.

II. EXPERIMENTAL PROCEDURES

The alloys studied can be represented by $Cu_{3-x}Mn_xAl$ with $0 < x < 1$. In the text, the alloys are designated by the x values ($x = 0$ for Cu_3Al and $x = 1$ for Cu_2MnAl). Table 1 summarizes the compositions of the alloys studied.

The alloys were prepared by melting 99.999% Cu, 99.9% Mn and 99.999% Al in an induction furnace under a helium atmosphere and were chill cast into a copper mold. Chemical analysis verified to within 1 weight % the compositions given in Table 1.

TABLE 1

Atomic and Chemical Compositions of the Alloys Studied

Atomic Composition	Estimated Compositions wt % Cu	Wt % Mn	wt % Al	x
Cu_3Al	87.6	----	12.4	0
$Cu_{2.8}Mn_{0.2}Al$	82.4	5.1	12.5	0.2
$Cu_{2.5}Mn_{0.5}Al$	74.3	13.1	12.6	0.5
$Cu_{2.2}Mn_{0.8}Al$	66.4	20.8	12.8	0.8
$Cu_{2.1}Mn_{0.9}Al$	63.5	23.6	12.9	0.9
Cu_2MnAl	60.9	26.2	12.9	1.0

The ingots were homogenized for three days at 850°C and oil quenched in order to avoid quenching cracks. Thin slices, 0.5mm thick, were then cut, homogenized at 850°C for 10 min. in a vertical resistance air furnace and quenched in iced brine to avoid precipitation of the high temperature phases and also to minimize the decomposition of the alloys inside the miscibility gap that exists at temperatures below 350°C. The alloys were then aged in oil baths at temperatures below 250°C and in salt baths (50% potassium nitrate - 50% sodium nitrate) above 250°C.

Electron microscope disc specimens, 2.3mm in diameter, were spark eroded from the heat-treated discs, thinned in an automatic jet polisher(12) and examined in a Siemens Elmiskop IA microscope operated at 100 kV.

III. CRYSTALLOGRAPHY OF THE $(Cu\text{-}Mn)_3Al$ ALLOYS

The ordering sequence of the middle alloy x = 0.5 is shown schematically in Fig. 1. The high temperature bcc disordered structure of the β phase orders first to the B2 structure. Al lower temperatures, the B2 structure further orders to an ordered solid solution (DO_3-$L2_1$) based on the DO_3 structure of Cu_3Al and the closely related $L2_1$ structure of Cu_2MnAl. The DO_3 and $L2_1$ superstructures consist of four interpenetrating fcc sublattices(13) two of which are occupied by Cu atoms (the unmarked corner sites in Fig. 1. The third sublattice (Δ) is occupied by Al atoms whereas the fourth sublattice is occupied by a random mixture of the remaining Cu and Mn atoms and its composition is determined by the composition of the alloy. Along the tie-line Cu_3Al-Cu_2MnAl, the composition of the fourth sublattice gradually changes from Cu to Mn. Decomposition of the single phase ordered solid solution (DO_3-$L2_1$) into a two phase mixture of Cu_3Al-rich DO_3 regions and Cu_2MnAl-rich $L2_1$

regions is accomplished solely by the decomposition of the fourth sublattice into a Cu-rich sublattice and a Mn-rich sublattice (Fig. 1).

The two possible types of APB vectors in the DO_3 and the $L2_1$ are $\frac{1}{4}a<111>$ and $\frac{1}{2}a<100>$. These are shown in Fig. 1.

IV. RESULTS AND DISCUSSION

A. Ordering and Decomposition

1. Ordering Temperatures

Thermal analysis was carried out to determine the two ordering temperatures of the alloys and the results are summarized in Fig. 2. The results for the Cu_2MnAl alloy are comparable to those obtained by other workers(4,5,6). Two thermal arrests of different magnitudes were observed in alloys having an atomic fraction of Mn $x \geqslant 0.5$ and they are associated with T_cB2 and T_cL2_1. The magnitude of the thermal arrest associated with the B2 ordering reaction increases with the Mn content. In the alloys $x < 0.2$, the thermal arrest associated with the B2 ordering reaction was too small to be observed. In the Cu_3Al alloy ($x = 0$), two thermal arrests were observed; that of the $B2 \rightarrow DO_3$ ordering reaction and that at 350°C which corresponds to the M_s temperature in this alloy(14).

2. The As-quenched Alloys

Two types of microstructures have been observed in quenched $(Cu-Mn)_3Al$ alloys; those containing martensite and those containing the untransformed ordered β phase. The martensitic phases of the binary Cu-Al system are well documented(14-15). It was found that the M_s temperature of the Cu_3Al alloy gradually decreases by the addition of Mn. Isolated martensite plates were observed in the as-quenched alloy $x = 0.2$, but not in the as quenched alloy x = 0.5.

The as-quenched non-martensitic alloys show tweed contrast microstructures and correspondingly, their diffraction patterns show diffuse scattering. These effects appeared to decrease with Mn content. Typical examples are shown in the micrograph and diffraction pattern of the as-quenched symmetrical alloy (x = 0.5) in Fig. 3. These features are similar to those of many age-hardenable alloy systems. They suggest the presence of dense arrays of fine coherent precipitates exhibiting strain contrast and will be discussed in Sec. IV-D.

3. Early Stage of the Decomposition

It was found that the alloys briefly aged well inside the miscibility gap decompose by forming composition modulations parallel to the cube planes of the matrix. Evidence of the decomposition is first resolved in diffraction patterns. Figs. 4(a) and (b) show the influence of aging on the (001) diffraction pattern of the alloys x 0.5 and 0.8. Diffuse streaking parallel to cube directions having the shape of an heraldic cross *patée* around all (hko) reflections can be resolved. During further aging, well defined satellites emerge from the diffuse cross *patée* (see Fig. 4).

The early stage of the decomposition inside the miscibility gap is metallographically consistent with that expected in the early stage of spinodal decomposition, or of a homogeneous phase transformation. The differences between the two mechanisms are purely thermodynamical and they cannot be distinguished metallographically(16). The diffraction effects produced by both mechanisms are also very similar(17) and cannot be distinguished by electron diffraction. The theoretical treatment of spinodal decomposition has been given by Hillert, Hilliard and Cahn and the important features of the transformation have been reviewed by Cahn(18) and more recently by Hilliard(19) and de Fontaine(20).

During the early stage of the decomposition, the compositional changes inside the spinodal can be described by a linear diffusion equation which when solved leads to the expression:

$$A(\beta,t) = A(\beta,0) \exp [R(\beta)t] \qquad (1)$$

where $A(\beta,t)$ is the amplitude of the Fourier component of wave number β at time t ($\beta = 2\pi/\lambda$ where λ is the wave length) and $R(\beta)$ is the amplification factor(19,21).

Since the diffraction pattern is a Fourier transform of the crystal(18,22), the Fourier spectrum expressed in equation (1) for a modulate structure corresponds to the appearance of diffuse intensity around the transmitted and diffracted electron beams. This diffuse intensity arises from the range of <100> compositional wave lengths (or wavevector β) present during the early stage of the decomposition. The Fourier spectrum of the modulated crystal (i.e. the diffuse intensity of the cross patée) has two components: a) the radial component describing the range of initial wavelengths and b) the tangential component describing the range in orientation of the waves(21). The arms of the crosses patée are aligned parallel to the cube directions and the range of orientations of the wave vector β (the tangential component of the Fourier spectrum) gradually decreases with aging. Cahn(23) has shown that in cubic crystals, the introduction of an elastic term in the diffusion equation favors the formation of {100} plane waves if the elastic constants are anisotropic, and if $2\,C_{44} > C_{11} + C_{12}$. It is believed that the increase in the anisotropic elastic energy during the decomposition causes the observed decrease in the radial component of the Fourier spectrum.

After a very short aging time, the exponential dependence of the amplitude on R(β) in equation (1) is expected to cause a dominance of components with wave numbers clustered around the modulation possessing maximum amplitude βm(18,19,20). This is well illustrated in Figs. 4(a) and (b) for the alloys x = 0.5 and 0.8 respectively where discreet "side band" satellites gradually emerge from the continuous diffuse intensity of the cross patterns. This behaviour is characteristic of spinodally decomposed alloys.

In <111> foils, the distribution of intensity of satellites in the alloy x = 0.5 aged at 200°C was symmetrical, whereas at 300°C the distribution was asymmetrical. This suggests that the three <100> directions of growth are equally favored at 200°C but not, at 300°C. It has been suggested(24) that this effect may arise from the influence of the small magnetic fields generated by the heating elements inside the oven during aging. This is possible since the aging temperature (300°C) is close to the Curie temperature of the Cu_2MnAl component (T_c = 360°C(25,26)). This is also consistant with the theory of magnetic aging of spinodal alloys developed by Cahn(27).

4. The Growth Stage

The inter-satellite spacing decreases with further aging (see Fig. 4). This is caused by a gradual increase in the compositional wavelength λ. The sequence of bright field images in Fig. 5 shows the gradual increase in λ during the growth stage of the decomposition and evidence for antiphase domain boundaries (APB's). This modulated microstructure was also observed to exist up to the grain boundaries indicating the homogeneous nature of the transformation.

Kinetic measurements of the early growth of the wavelength in the alloy $x = 0.5$ are summarized in Fig. 6 where the value of λ was calculated from at least ten independent diffraction patterns(28,29). The relationship between log λ and log t is linear and can be represented by:

$$\lambda = kt^n \tag{2}$$

where $n = 0.127$, 0.172 and 0.216 at 200°C, 240°C and 300°C respectively.

The time dependence of the growth is weaker than that predicted by the theory of coarsening ($n = 1/3$)(30,31). The spinodal structure in Cu-Ni-Fe alloys, and precipitates in Ni-Al alloys were found to coarsen at a $t^{1/3}$ rate(16,18). Thus our results do not support the particle coarsening law during the early and intermediate stages of decomposition, but they are in agreement with the predicted shift toward longer wave lengths(21). The variation of n with temperature can be explained by enhanced growth caused by a) the decreasing importance of the $L1_0$ phase discussed later, or b) the increasing importance of magnetic aging with temperature. The latter mechanism has been discussed in the previous paragraphs.

The APB's of the as-quenched alloys were smoothly curved and they remained smoothly curved during short aging at temperatures well inside the miscibility gap even though the microstructure is modulated. A striking example of this behaviour is shown in Fig. 7 where the smoothly curved APB's and the composition modulations are imaged simultaneously.

In this [01$\bar{1}$] foil, the (100) composition modulations parallel to the electron beam show greater contrast than those parallel to (010) and (001) which are oriented at 45° to the electron beam. The modulations are imaged by double diffraction of the (022) fundamental reflection. The isotropic behaviour of APB's observed in microstructures aged up to 40 min. at 300°C (λ average = 300Å) indicates that there is little interaction between the APB's and the modulated structure during the early stages of decomposition.

5. Coarsening

The wavelength of the decomposition products continues to increase with further aging inside the miscibility gap. Typical coherent microstructures of the alloy x = 0.5 aged at 300°C for 1,400 min. and 2,000 min. are presented in Fig. 8(a) and (b). In this symmetrical alloy (equal fractions of the two phases), the decomposition produces <100> oriented coherent rod-like particles and Fig. 8 shows the preferential electropolishing of one component. In (a), the rods are parallel to the [010] direction and also parallel to the foil surface (001) whereas in (b), the particles are oriented at 45° to the (011) foil surface and, therefore, the shortened rods appear as overlapping discs.

The wavelengths were found to vary quite widely during coarsening. In Fig. 8(b), regions with wave length of 2,000Å are often separated by regions having an apparent wavelength of 150-200Å. This striking feature gives rise to a fully coherent convoluted microstructure. In the asymmetrical alloys x = 0.8 and 0.9, the minor phase form thin coherent platelets parallel to the cube planes of the matrix.

The coarsening model that best fits our results is that proposed by Swanger et al.(32). Their computer simulations have shown the influence of the gradient energy term in the solution of the non-linear diffusion equation. They consider four stages during the growth of the modulations. It appears that when the amplitude of sinusoidal modulations approaches the spinodal boundary, the importance of the gradient energy term increases especially near the interface and causes preferential growth of the amplitude which results in the squaring of the modulation. This corresponds to stage 1 and 2. During stage 3, the composition of the corners (near the interface) crosses the spinodal boundary which results in a convoluted microstructure. Particle coarsening occurs during stage 4. Thus, it appears that in the alloy x = 0.5 the growth of the small wavelength modulations can be explained by the interfacial composition gradient causing an increase of the gradient energy term in the non-linear diffusion equation. The lever rule is obeyed by the generation of amplitudes of the "opposite" composition and also by the slower crossing of the spinodal boundary within the particles where the gradient energy term has little favorable influence. Eventually, particle coarsening occurs as illustrated by the absence of small wave lengths in the alloy x = 0.5 aged at 300°C for 7,000 min. or longer.

B. Loss of Coherency

The symmetrical alloy x = 0.5 loses coherency at wavelengths larger than 2,000Å. There are two mechanisms for the loss of coherency in this alloy; a) the generation of interfacial plate-like precipitates (the precipitates P in Fig. 9 to be discussed elsewhere and b) the generation of $\frac{1}{2}a\langle 100\rangle$ edge dislocations (see Fig. 9) as has been discussed in a previous paper(33). Fig. 9 clearly shows an equiproportion of the two components indicating that the alloy x = 0.5 is near the center of the miscibility gap. It can also be seen that component marked B exhibits a "tweed-like" texture. This feature will be discussed in Section D-2.

The morphological changes during coarsening are accompanied by changes in diffraction patterns. This illustrated in the two (100) diffraction patterns of the alloy x = 0.5 in Fig. 10(a) and (b) obtained respectively before and after the loss of coherency. Well before interfacial dislocations are observed, the diffracted spots are elongated and sometimes doubled in directions orthogonal to the rod axis. For simplicity, the magnitude and direction of the splitting are indicated by the magnitude and direction of the arrows in Fig. 10(a). The area marked in Fig. 10(a) is schematically reproduced in Fig. 11(a) and the splitting is interpreted in terms of a two-phase microstructure containing a cubic phase and a tetragonal phase. The c/a ratio of the tetragonal phase measured from diffraction patterns is 1.033 ± 0.005 with the c axis parallel to the rod axis. The image corresponding to the (100) diffraction pattern in Fig. 11(a) is shown in Fig. 8(a). Dark-field experiments have shown that the tetragonal phase is the Cu_3Al-rich phase. The streaks through (000) and (002) type reflections in Fig.10 are believed to arise from double diffraction at the coherently strained interface.

Fig. 11(a) indicates that the metastable tetragonal phase arises from an expansion of the unit cell of the Cu_3Al-rich phase preferentially in the c direction, the rod axis.

After loss in coherency, the streaking is not observed and all spots are doubled in the direction parallel to the reciprocal lattice vector $\vec{g}$. In addition, the magnitude of this doubling increases radially with increasing $\vec{g}$, as shown in Fig. 10(b). This indicates that the two phases are cubic but with different lattice parameters as sketched in Fig. 11(b). The image corresponding to the (100) diffraction pattern in Fig. 11(b) is shown in Fig. 9.

The estimated value of the misfit for the symmetrical alloy fully developed at 300°C (1.57 ± 0.15%) is consistant with Cu_3Al-rich and Cu_2MnAl-rich product phases.

After loss of coherency, the volume of the unit cell of the Cu_2MnAl-rich component is related to that of the Cu_3Al-rich component by the expression:

$$V_{Cu_2MnAl} = V_{Cu_3Al}(1 + \delta)^3 \qquad (3)$$

where δ, a fractional dilation of the lattice, is a function of composition which in turn is a function of the decomposition temperature. If these two phases were coherent, the state of the coherency strain at the interface would be purely dilatational. However, before the loss of coherency, the lattice parameters of the two phases are identical only in the direction of the rod axis giving rise to the tetragonal phase (Fig. 10 and 11). This direction of best fit corresponds to the direction of easy growth at the rod-shaped particles(34). A similar tetragonal distortion prior to the loss of coherency in Cu-Ni-Fe was reported by Butler and Thomas(29). When coherency is lost the interfacial dislocations must relieve the dilatational strain at the interface for the correct matching of the lattice planes of the adjoining cubic phases. In smoothly curved interfaces, this is accomplished by formation of a network of three orthogonal sets of parallel $\frac{1}{2}a\langle 100\rangle$ edge type dislocations(33).

In the ternary-rich asymmetrical alloys x = 0.8, 0.9, the minor phase has a plate-like morphology (see Fig. 12). Diffraction experiments also suggest the presence of a Cu_2MnAl-rich matrix and Cu_3Al-rich minor phase.

Contrast experiments have shown that the dislocations at the planar interface are similar to those found in the symmetrical alloy. Fig. 12 is a bright-field-dark-field pair of micrographs showing the presence of interfacial dislocations only in certain areas of the interface. In addition, this figure shows that rapid thickening of a plate occurs only near the dislocated areas of the interface. This localized accelerated coarsening was also observed in the spinodally decomposed Cu-Ni-Fe alloys by Butler and Thomas(29) and can be attributed to the increased rate of relief of interfacial strain resulting from the generation of dislocations.

C Nucleation and Growth of Cu_2MnAl-rich Particles

Heterogeneous nucleation of Cu_2MnAl-rich precipitates was observed in the binary-rich asymmetrical alloy x = 0.2 aged at a temperature just below the miscibility gap (See Fig. 13). The bright field micrograph in (a) shows the early stage of the heterogeneous precipitation. The $\frac{1}{4}a\langle 111\rangle$ type APB's are in contrast in (b) whereas, both types of APB's {the $\frac{1}{4}a\langle 111\rangle$ and the $\frac{1}{2}a\langle 100\rangle$} are in contrast in (c). A comparison of the three micrographs reveals that the Cu_2MnAl-rich precipitates in (a) nucleate preferentially at $\frac{1}{4}a\langle 111\rangle$ APB's imaged in (b). The coarsening of the precipitates is characterized by the formation of rows of

Cu_2MnAl-rich cubes paralled to the <100> directions of the Cu_3Al-rich matrix.

Swann$^{(35)}$ also observed the heterogeneous precipitation of a γ-type phase at both types of APB's in a Cu-Ni-Al alloy having the DO_3 structure and he suggests that the driving force for nucleation comes from the APB energy itself. In a related study of the annihilation characteristics of APB's in the alloy x = 0.5, we found that the energy of the $\frac{1}{4}$a<111> APB's is 25% larger than the energy of the $\frac{1}{2}$a<100> APB's. This is consistent with our observation that the B2 ordering temperature T_cB2 is higher than T_cL2_1-DO_3. It is therefore energetically more favorable to form stable nuclei of the precipitated phase at $\frac{1}{4}$a<111> than at $\frac{1}{2}$a <100> APB's.

In contrast to the nucleation and growth behaviour of the asymmetrical alloy x = 0.2, no heterogeneous precipitation at APB's was observed in alloys aged well inside the miscibility gap. This is illustrated in the (111) dark field micrograph of Fig. 7 showing both the anisotropic composition modulation and the isotropic $\frac{1}{2}$a<100> APB's, as expected after spinodal decomposition.

D. Further Decomposition of The Cu_3Al-Rich Phase

1. The $L1_0$ Phase

The diffraction patterns of alloys aged well inside the miscibility gap show extra reflections. The extra reflections become more diffuse with increasing aging temperature (240°C to 300°C). Typical examples of discrete and diffuse extra reflections in alloy x = 0.8 are shown in Figs. 14 and 15 respectively. A comparison of Figs. 15(a) and (b) reveals that the intensity of the extra reflections in the (001) diffraction pattern increases when the foil is slightly tilted from the exact (001) orientation. This behaviour is similar to that observed by Delaey et al. in beta-brass type alloys(36). The extra reflections can be indexed in terms of two phases; the ω-phase reported by Delaey et al.(36) and related to the Cu-Al martensites and a new phase having the $L1_0$ superstructure and referred to as the $L1_0$ phase in this paper. The diffraction effects caused by these two phases are very similar in <001> diffraction patterns but very dissimilar in <110> diffraction patterns. The <110> diffraction pattern in Fig. 14(b) contains only $L1_0$ extra spots. Selected dark-field experiments revealed that the $L1_0$ reflections in Fig. 14(a) come from two $L1_0$ variants marked (1) and (2) and having mutually orthogonal C axes. The $L1_0$ reflections in (b) come from only one $L1_0$ variant. The extra reflections are elongated in a direction normal to the C axis of the $L1_0$ phase.

The diffraction results suggest that the $L1_0$-matrix orientation relationship is that shown in Fig. 16. The solid lines indicate the unit cell of the ordered DO_3 matrix and the dashed lines indicate the unit cell of the proposed $L1_0$ phase. The important features of the proposed $L1_0$ phase are summarized as follows:

a) The $L1_0$ structure consists of alternate stacking of A and B {001} planes perpendicular to the (tetragonal) C axis.

b) The C axis of the $L1_0$ phase lies near one of the six <110> directions of the matrix. Furthermore each C axis orientation can be shared by two APB related variants thus producing a total of twelve possible $L1_0$ variants. Each of the three pairs of variants having their C axis in one of the three {100} type planes are twin related within that plane {see Fig. 14(a) and (c)}.

c) Measurements from diffraction pattern revealed that there is a near correspondence of atomic positions between the $L1_0$ structure and the matrix structure. The dimensions of the $L1_0$ unit cell estimated from the Cu_2MnAl matrix unit cell are:

$A = 4.24$ A

$B = 2.97$ A

$C = 4.24$ A

The C axis is normal to the AB stacking sequence and does not correspond to the shortest dimension of the unit cell.

The morphology of the $L1_0$ phase was studied by selected dark field microscopy. The bright field micrograph of the alloy $x = 0.8$ aged at 240°C for 10,000 minutes shown in Fig. 17 reveals the preferential polishing of a plate-shaped component. The corresponding dark-field micrographs in (b) and (c) [from the same foil as in (a)] show the variants (1) and (2) respectively. It can be seen that the $L1_0$ particles are elongated in the direction of their respective C axis thus producing the streaking of the $L1_0$ reflections observed in Fig. 15(a)(28).

The dark-field micrographs in Fig. 17(b) and (c) also show that twin related $L1_0$ variants grow in closely related groups suggesting a highly interconnected arrangement of the particles. In each group, Fig. 17 shows that the space unoccupied by variant (1) is partially occupied by variant (2). It was also observed that the volume fraction of the $L1_0$ variants differ markedly from area to area in the foil.

The $L1_0$ particles are distributed in platelets parallel to the (001) plane of the matrix. The dark-field micrograph from a (110) foil in Fig. 18 was obtained using the $L1_0(110)_1$ reflection in Fig. 15(b). The micrograph shows that the platelets parallel to the (001) plane of the matrix are 100-200Å thick and 400-500Å apart. The particles of variant (2) are believed to be located between those of variant (1) and within the same platelet.

The dark field images e.g. Fig. 18, 19 show that the volume fractions and size of different variants of the $L1_0$ phase vary even in the same alloy. This suggests that a favorable growth variant for $L1_0$ may develop similarly to that due to magnetic effects also found in these alloys. A difficulty exists in [001] orientations due to superposition of reflections (e.g. $L1_0$ and ω phase spots).

The above dark-field analysis indicates that the $L1_0$ phase form three sets of platelets parallel to the cube planes of the matrix. Each {001} platelet contains two twin related $L1_0$ variants having their c axes parallel to the two <110> directions of the matrix that are parallel to the platelets.

The interface of APB related variants is characterized by the wrong stacking sequence of AB planes (e.g. ABABBABA). This situation is similar to that found in Cu-Au and may result in a long period superlattice LPS$^{(37)}$. The interface between two APB variants is a $\frac{1}{2}a\langle 101\rangle$ or $\frac{1}{2}a\langle 011\rangle$ APB of the $L1_0$ structure. In $(201)L1_0$ dark-field micrographs the APB is expected to show dark contrast since α, the phase angle across the APB $=2\pi g.R = \pi(201).(101) = \pi^{(13)}$. We believe that the closely spaced dark fringes in the dark field micrograph in Fig. 19(a) is evidence of the LPS in the $L1_0$ phase. The contrast at APB's is very sensitive to the diffraction conditions(13) and may vanish when the foil is tilted {Fig. 19(b)}. This observation further supports the finding that the fringes are caused by APB contrast inside the $L1_0$ particles, because such contrast can only come when using $L1_0$ reflections. It was found that the period of the LPS is constant within each platelet of the $L1_0$ phase, but varies between 60Å to 110Å from platelet to platelet.

In order to determine the origin of the $L1_0$ phase, the symmetrical alloy $x \doteq 0.5$ was first aged at 300°C for 18,000 minutes and further aged at 240°C for 1300 minutes. The first aging produces the double cubic structure whereas lower temperatures, one of the two components transforms. Two characteristic features of the low temperature transformation were observed. Firstly, the microstructure is characterized by the presence of a high density of martensite plates in the Cu_3Al-rich phase (labelled B in Fig. 20). Secondly, in small areas of the foil <u>not</u> transformed to martensite e.g. Fig. 20(b) the component labelled B shows a modulated structure in bright-field similar to that caused by the $L1_0$ structure and/or the ω type phase in asymmetrical alloys. Selected dark-field microscopy has shown that the component B possess the smaller lattice parameter associated with the Cu_3Al-rich phase. This result suggests that at temperatures well inside the miscibility gap, the decomposition proceeds by the formation of compositional modulations of cubic Cu_2MnAl-rich particles coherent with Cu_3Al-rich regions having the $L1_0$ structure and/or the ω type structure.

2. The "Tweed-Like" Texture

The symmetrical alloy x = 0.5 aged at temperatures near the miscibility gap shows diffuse streaking and extra diffuse reflections in diffraction patterns and the image contrast exhibits "tweed-like" texture (see Fig. 16 and 10). These features are similar to those observed in the as-quenched alloys described in Section I.

Diffuse maxima are resolved along the length of the <110> diffuse streaks. These maxima are centered around the position of the $L1_0$ reflections in reciprocal space. A dark field micrograph obtained using the $(201)_{L1_0}$ reflection in Fig. 15(b) is shown in Fig. 21(b) and compared to the corresponding bright field image in Fig. 21(a). Fig. 21 reveals that the component B exhibiting the "tweed-like" texture contains a high density of fine coherent particles as evidenced by the white dotted contrast in dark-field. Selected dark field microscopy revealed that the component B possess the smaller lattice parameter associated with the Cu_3Al-rich phase. This observation and the results given in the previous section suggest that at temperatures close to the miscibility gap, the Cu_3Al-rich phase is composed of a high density of fine coherent $L1_0$ regions embedded in a cubic DO_3 superstructure. Similar structures have been observed in a number of ordered alloys(38,39,40). These observations suggest the presence of the $L1_0$ phase field at the binary-rich end of the miscibility gap.

3. The DO_3-$L1_0$ Transformation

The proposed structure of the $L1_0$ phase may be generated from the DO_3 structure simply by the partial disordering of the DO_3 lattice to the B2 lattice followed by the ordering of only one set of the {110} planes of the B2 structure. This is equivalent to the generation of non-conservative $\frac{1}{4}a\langle 111\rangle$ APB's of the DO_3 structure parallel to every (220) planes of the DO_3 structure(39,41) as illustrated in Fig. 22. This structural interpretation of phase relations was illustrated by Okamoto and Thomas(39) in Ni-Mo alloys. In the DO_3 structure, the two APB's (220) $\frac{1}{4}a[111]$ and $(220)\frac{1}{4}a[11\bar{1}]$ are nonconservative and the proposed $L1_0$ structure is equivalent to the random distribution of the above two APB's at every (220) plane of the transforming crystal (Fig. 22).

The above discussion illustrates that the proposed $L1_0$ structure can be generated from the DO_3 structure. However, since the alloy contains three elements, there are a large number of atomic combinations that can produce the AB stacking sequence of the proposed $L1_0$ structure.

In Section III, we have proposed a simple model of the decomposition inside the miscibility gap. The model involves interdiffusion of atoms occupying only one of the four sublattices of the DO_3 superstructure. The model appears to be correct during the early stages of the decomposition at temperatures just inside the miscibility gap. However, at lower temperatures, the model is no longer valid since the ordering of the {220} planes of the Cu_3Al-rich component requires at least partial diffusion of atoms occupying all four sublattices of the DO_3 superstructure.

4. Overaging

Still further decomposition occurs upon overaging alloys rich in manganese ($x \gtrsim 0.5$) inside or outside the miscibility gap. The details of this transformation will be discussed in a separate paper, but it is useful to indicate here that the decomposition involves precipitation of the γ phase similar to Cu_9Al_4 (35,42,43). Detailed analysis of this transformation suggests that the decomposition tie line is not along Cu_3Al-Cu_2MnAl, but rotates towards Cu_9Al_4-$Cu_{2.2}MnAl_{0.8}$ as shown in Fig. 23.

V. SUMMARY

The alloys along the composition tie line Cu_3Al-Cu_2MnAl order during quenching to a DO_3-$L2_1$ ordered phase. At temperatures below 325°C, the alloys decompose within a miscibility gap into Cu_3Al-rich and Cu_2MnAl-rich particles. The early metallographic aspects of the decomposition resemble those of a spinodal decomposition, e.g. <100> composition modulations, and cross-shaped diffuse sideband scatter in diffraction patterns are observed.

The binary-rich end of the miscibility gap interacts with an additional phase field characterized by an $L1_0$ superstructure. This $L1_0$ phase field strongly influences the transformations of the Cu_3Al-rich phase during spinodal decomposition.

The symmetrical alloy $Cu_{2.5}Mn_{0.5}Al$ alloy is of particular interest. This alloy decomposes along the tie line Cu_9Al_4 - $Cu_{2.2}MnAl_{0.8}$. At temperatures well inside the miscibility gap, the Cu_3Al-rich product phase passes an $L1_0$ structure whereas at temperatures close to but within the miscibility gap, it consists of a dense array of fine $L1_0$ regions coherent with the DO_3 matrix. At all temperatures, the Cu_2MnAl-rich phase possess the cubic $L2_1$ structure. The wavelength of the composition modulations gradually increases forming rod-shaped particles and at about 2000Å, the coherency is lost primarily by the generation of interfacial dislocations. However, prior to the loss of coherency, the coexistence of large and small modulations form a highly convoluted microstructure. At that stage, the Cu_3Al-rich rods possess a tetragonally distorted DO_3 structure whereas the Cu_2MnAl-rich rods possess the cubic $L2_1$ structure. Both phases are cubic after the loss of coherency.

In the aged ternary-rich asymmetrical alloys, the Cu_3Al-rich minor phase grows in {100} oriented plates and no tetragonal distortion was observed.

In the binary-rich asymmetrical alloy $Cu_{2.8}Mn_{0.2}Al$ aged at temperatures close to the miscibility gap, the Cu_2MnAl rich minor phase heterogenously nucleates at quenched in 1/4a<111> APB's and grow into<100> oriented rows of cuboids.

ACKNOWLEDGMENTS

This work was supported by the U.S. Energy Research and Development Administration. M.B. gratefully acknowledges the award of a Fellowship by Hydro-Quebec and SIDBEC-DOSCO Montreal, Canada.

FIGURE CAPTIONS

Fig. 1. Schematic representation of the ordering sequence of the quenched $Cu_{2.5}Mn_{0.5}Al$ alloy (vertically) and its isothermal decomposition (horizontally).

Fig. 2. The ordering temperatures $T_c(B2)$ and $T_c(DO_3\text{-}L2_1)$ and the miscibility gap of the $(Cu\text{-}Mn)_3Al$ alloys respectively determined by thermal analysis and electron microscopy.

Fig. 3. Bright field micrograph (a) and the (001) diffraction pattern (b) of the quenched $Cu_{2.5}Mn_{0.5}Al$ ($x = 0.5$) alloy showing a "tweed-like" microstructure and diffuse streaking.

Fig. 4. Sections of (001) diffraction patterns obtained after aging the alloys $Cu_{2.5}Mn_{0.5}Al$ ($x = 0.5$) in (a) and $Cu_{2.8}Mn_{0.2}Al$ ($x = 0.8$) in (b) at 200°C for times indicated in minutes. The figure illustrates the gradual emergence of the well defined satellites from the diffuse intensity of the cross <u>patée</u> and the gradual decrease of the intersatellite spacing with increasing aging time. This is best observed around the (200) superlattice reflection in center.

Fig. 5. Bright field micrographs from the alloy $Cu_{2.2}Mn_{0.8}Al$ ($x = 0.8$) aged for (a) 30 sec. (b) 1 min. and (c) 2 min. showing the gradual increase of the wavelength of the composition modulation parallel to the cube planes. Note the fringe contrast at APB's possibly due to segregation during the quench ($\vec{g} = 220$).

Fig. 6. A log λ vs log t plot obtained from intersatellite spacings in diffraction patterns of the alloy $Cu_{2.5}Mn_{0.5}Al$ aged at 200°C, 240°C and 300°C.

Fig. 7. (111) dark field micrograph of the alloy $Cu_{2.5}Mn_{0.5}Al$ ($x = 0.5$) aged at 300°C for 30 sec. showing the smoothly curved 1/2a<100> APB's and the anisotropic composition modulations.

Fig. 8. Bright field micrographs of the alloy $Cu_{2.5}Mn_{0.5}Al$ aged at 300°C for 1,400 min. in (a) and 2,000 min. in (b) showing the coherent rod-like particles with their long axis parallel to the cube directions. In (a), the rods are parallel to the foil whereas in (b), they are oriented at 45° to the foil surface. In both micrographs the large modulations are often separated by small modulations.

Fig. 9. Bright field micrograph of the alloy $Cu_{2.5}Mn_{0.5}Al$ ($x = 0.5$) aged at 300°C for 10,000 min. showing the fully developed microstructure. Note the presence of interfacial dislocations and the "tweed-like" texture of the Cu_3Al-rich component labelled B.

Fig. 10. (100) diffraction patterns of the alloy $Cu_{2.5}Mn_{0.5}Al$ aged at 300°C for 1000 min. in (a) and 10,000 min. in (b) obtained before and after the loss of coherency respectively. Figure 10(a) corresponds to Fig. 8(a) and 10 (b) corresponds to Fig. 9. The magnitude and direction of the arrows indicates the magnitude and direction of the splitting of reflections. The interpretation of the diffraction patterns is given in Fig. 11 (see text).

Fig. 11. Schematic representation of the marked areas in Fig. 10. The splitting observed before loss of coherency in (a) is interpreted in terms of a cubic Cu_2MnAl-rich phase coherent with a tetragonal Cu_3Al-rich phase. After loss of coherency both phases have cubic structures (see b).

Fig. 12. Bright field and dark field micrographs of the asymmetrical alloy $Cu_{2.2}Mn_{0.8}Al$ (x = 0.8) aged at 315°C for 1100 min. showing partially dislocated interfaces. Note the more rapid thickening of the plates only in the dislocated regions of the interface.

Fig. 13. Corresponding micrographs from the asymmetrical alloy $Cu_{2.8}Mn_{0.2}Al$ (x = 0.2) aged at 240°C for 30 min. Note that the heterogeneous precipitates of the Cu_2MnAl-rich minor phase in (a) nucleate preferentially at the 1/4 a<111> APB's in (b) and possibly at the 1/2 a<100> APB's in (c).

Fig. 14. (001) and (110) matrix diffraction patterns from the alloy $Cu_{2.2}Mn_{0.8}Al$ (x = 0.8) aged at 240°C for 10,000 minutes. The extra reflections (in parenthesis) are indexed in terms of the proposed $L1_o$ phase. Two twin related variants (1) and (2) are diffracting in (a) whereas in (b), only the variant(1) is diffracting.

Fig. 15. (001) diffraction patterns of the alloy $Cu_{2.5}Mn_{0.5}Al$ (x = 0.5) aged at 300°C for 10,000 min. and showing diffuse streaking and diffuse $L1_o$ reflections. Note that the diffuse intensity increases when the foil is tilted slightly from the (001) orientation in (b).

Fig. 16. Schematic representation of the coherent lattice relationship between DO_3 and $L1_o$. The labelled atoms at lattice sites refer only to the DO_3 structure. Note that the $L1_o$ C axis normal to the AB stacking sequence is also normal to the smallest dimension of the unit cell.

Fig. 17. Micrographs from the alloy $Cu_{2.2}Mn_{0.8}Al$ aged at 240°C for 10,000 minutes. A typical bright field micrograph is shown in (a). The dark field micrographs in (b) and (c) were obtained using the $(201)_1$ and $(201)_2$ $L1_o$ reflections in Fig.14(a) and show the variants (1) and (2) respectively.

Fig. 18. Dark field micrograph showing the $L1_o$ variant (1) in a (110) foil of the alloy $Cu_{2.2}Mn_{0.8}Al$ (x = 0.8) aged at 240°C for 10,000 minutes. The image was obtained using the (110) $L1_o$ reflection in Fig.14(b) and shows that the $L1_o$ phase grows in platelets parallel to the cubic plane.

Fig. 19. (201) $L1_o$ dark field micrographs from the alloy $Cu_{2.2}Mn_{0.8}Al$ (x = 0.8) aged at 240°C for 10,000 minutes showing parallel dark fringes (see circled areas) in some areas of the $L1_o$ plates. A comparison of the circled areas in (a) and (b) reveals that the fringe contrast vanishes by changing slightly the diffraction conditions.

Fig. 20. Bright field micrographs of the alloy $Cu_{2.5}Mn_{0.5}Al$ (x = 0.5) aged at 300°C for 18,000 minutes and subsequently aged at 240°C for 1300 minutes. The figure shows the transformation of the Cu_3Al-rich component labelled B during the low temperature aging. In the area in (a) the Cu_3Al-rich

component transforms mostly to martensite whereas in b) it transforms mostly to the $L1_0$ phase.

Fig. 21. (220) bright field micrograph (a) of the alloy $Cu_{2.5}Mn_{0.5}Al$ (x = 0.5) aged at 300°C for 10,000 min. showing the "tweed-like" texture of the Cu_3Al-rich component labelled B. The corresponding dark field micrograph in (b) shows strong while dotted contrast only in the Cu_3Al-rich component characterized by the "tweed-like" texture.

Fig. 22. Illustration of the DO_3-$L1_0$ transofrmation by the generation of parallel nonconservative a/4<111> APB's at every {220} planes of the DO_3 structure. Five (001) atomic planes are shown and represented by various atom sizes. Note that there is no ordering of the {220} planes in the DO_3 structure. The faulted DO_3 structure in (b) is equivalent to the $L1_0$ structure described in the text where the $(2\bar{2}0)$ planes of the DO_3 structure order.

Fig. 23. The Cu-rich portion of the Cu-Mn-Al Gibb's triangle showing the limits of the miscibility gap estimated at 300°C and the decomposition tie-line of the symmetrical alloy $Cu_{2.5}Mn_{0.5}Al$ (x = 0.5) also estimated at 300°C.

REFERENCES

1. D. R. F. West and D. Lloyd Thomas, J. Inst. Metals, 85, 97 (1956-57).
2. G. B. Johnston and E. O. Hall, J. Phys. Chem. Solids, 29, 195 (1968).
3. R. Kimura, K. Endo and T. Ohoyama, J. Phys. Soc. Japan, 17, 723 (1962).
4. Y. E. G. Nesterenko, I. A. Osipenko and S. A. Firstov, Phys. of Metals and Metallography, 27, No. 1, 135 (1969).
5. J. P. Lisse and B. Dubois, Memoires Scientifiques Rev. Metallurg., LXVIII, No. 7-8 (1971).
6. M. Bouchard and P. R. Swann, 7th Int. Congress Electron Microscopy, (Grenoble, 1970), Soc. Francaise de Mic. Electron., 2, 475 (1970).
7. M. Bouchard and P. R. Swann, to be published.
8. A. J. Bradley and J. W. Rogers, Proc. Roy. Soc., 144A, 350 (1934).
9. K. Endo, T. Ohoyama and R. Kimura, J. Phys. Soc. Japan, 19 1494 (1964).
10. E. Persson, Z. Physik, 57, 115 (1929) (see Ref. 8).
11. D. P. Oxley, R. S. Tebble and K. C. Williams, J. Applied Phys., 34, No. 4, 1362 (1963).
12. R. D. Schoone and E. A. Fischione, Rev. Scientific Inst., 37, No. 10, 1351 (1966).
13. M. J. Marcinkowski, Electron Microscopy and Strength of Crystals, (Interscience, N.Y. 1962) G. Thomas and J. Washburn, Eds., p. 333.
14. P. R. Swann and H. Warlimont, Acta. Met., 11, 511 (1963).
15. S. Kajiwara, J. Phys. Soc. Japan, 22, 3, 795 (1967).
16. A. J. Ardell and R. B. Nicholson, Acta Met., 14, 1295 (1966).
17. Y. D. Tiapkin and M. V. Jibuti, Acta Met., 19, 365 (1971).

18. J. W. Cahn, Trans. AIME, 242, 166 (1968).

19. J. E. Hilliard, Phase Transformations, ASM, Metals Park, 497 (1970).

20. D. de Fontaine, Ultra Fine Grain Metals, Syracuse University Press 93 (1970).

21. J. W. Cahn, Acta Met., 14, 1685 (1966).

22. L. E. Tanner, to be published in Acta Met.

23. J. W. Cahn, Acta Met., 10, 179 (1962).

24. H. Warlimont (private communication).

25. K. Endo, T. Ohoyama and R. Kimura, J. Phys. Soc. Japan 19, 1494 (1964).

26. D. P. Oxley, R. S. Tebble and K. L. Williams, J. Appl. Physics, 54, No. 4, 1362 (1963).

27. J. W. Cahn, J. Appl. Phys. 34, 3581 (1963).

28. P. B. Hirsch, A. Howie, R. B. Nicholson, D. W. Pashley and M. J. Whelan, Electron Microscopy of Thin Crystals (London, Butterworths, 1965).

29. E. P. Butler and G. Thomas, Acta Met., 18, 347 (1970).

30. I. M. Lifshitz and V. V. Slyozov, J. Phys. Chem. Solids, 19, 35, (1961).

31. C. Wagner, Z. Electrochem, 65, 581 (1961).

32. L. A. Swanger, P. K. Gupta and A. R. Cooper, Jr., Acta Met., 18, 9 (1970).

33. M. Bouchard, R. J. Livak and G. Thomas, Surface Science 31, 275 (1972).

34. G. C. Weatherly, Phil. Mag., 17, 791 (1968).

35. P. R. Swann, Phil. Mag., 14, 461 (1966).

36. L. Delaey, A. J. Perkins and T. B. Massalski, J. of Materials Science, 7, 1197 (1972).

37. H. Sato and R. S. Toth, Alloying Behavior and Effects in Concentrated Solid Solutions, T. B. Massalski ed., Gordon and Breach, Science Publishers Inc., New York (1965).

38. H. Sato, R. S. Toth and G. Hondo, J. Phys. Chem. Solids, 28, 137 (1967).

39. P. R. Okamoto and G. Thomas, Acta Met., 19, 825 (1971).

40. S. K. Das, P. R. Okamoto, P. M. J. Fisher and G. Thomas, Acta Met. 21, 913 (1973).

41. J. B. Mitchell, Scripta Met., 4, 411 (1970).

42. A. J. Bradley, Phil. Mag., 6, 878 (1928).

43. A. J. Bradley, H. J. Goldsmidt and H. Lipson, J. Inst. Metals, 63, 149 (1938).

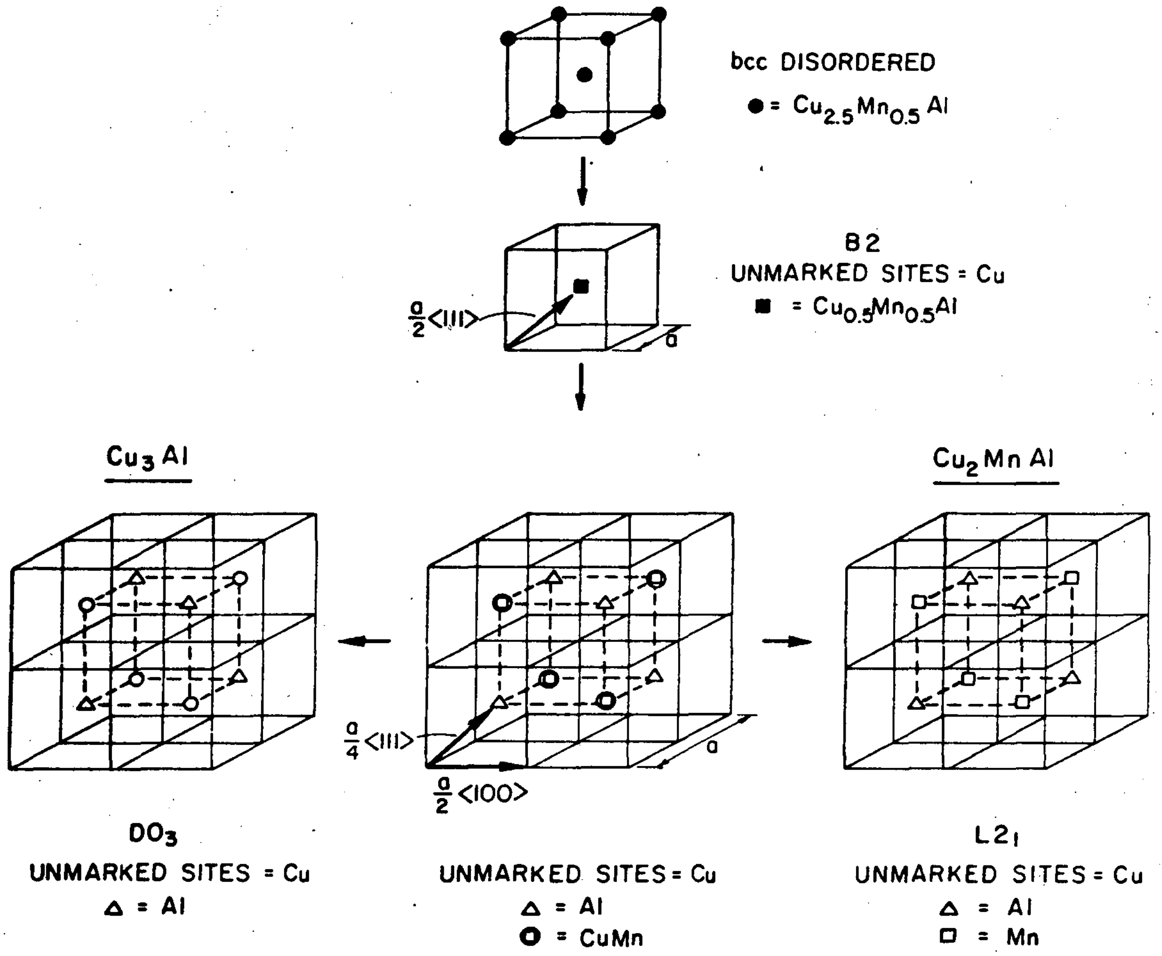

XBL 724-6199

Fig. 1

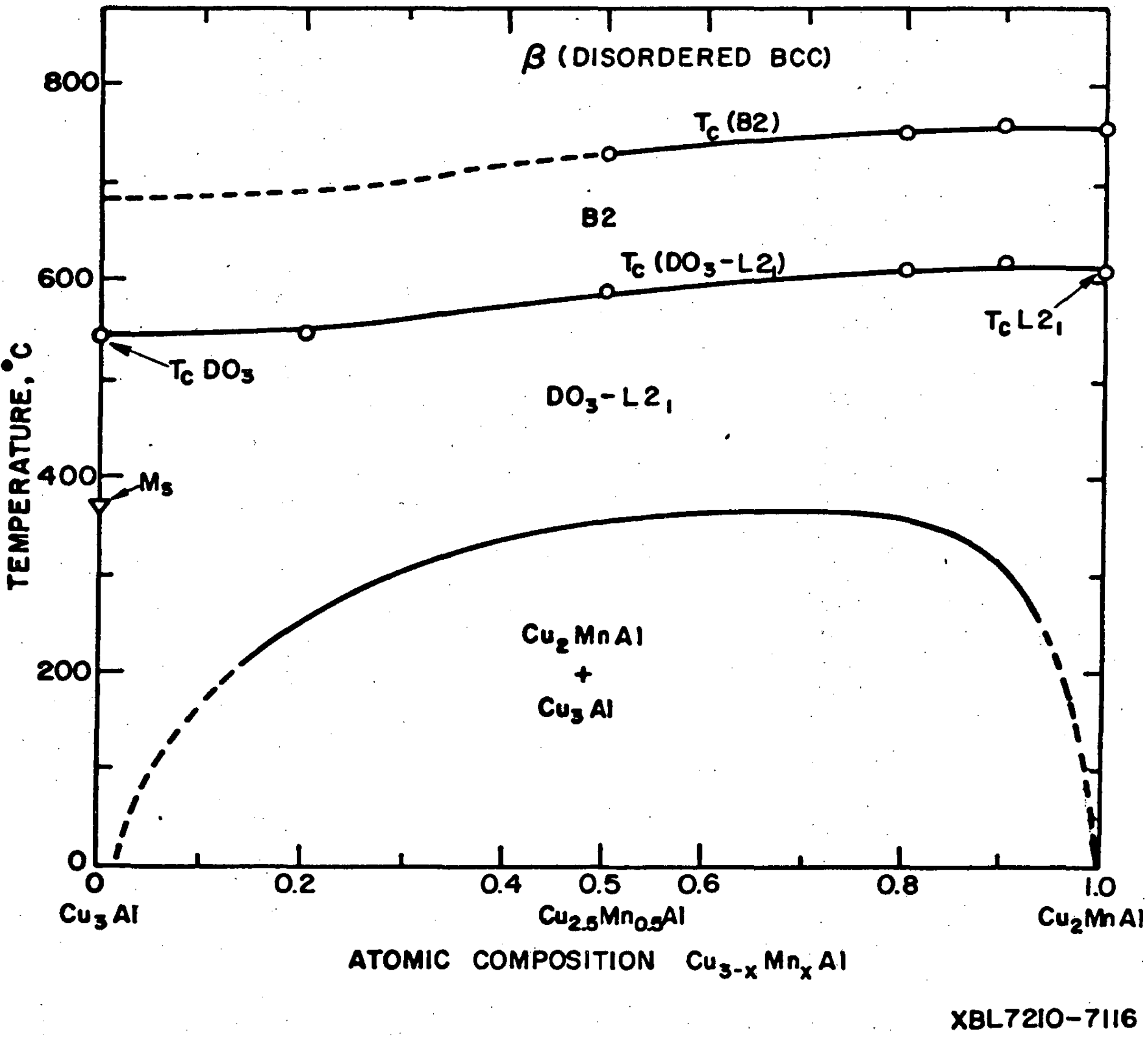
β (DISORDERED BCC)
T_c (B2)
B2
T_c (DO_3-$L2_1$)
T_c DO_3
T_c $L2_1$
DO_3-$L2_1$
M_s
Cu_2MnAl + Cu_3Al
TEMPERATURE, °C
0
200
400
600
800
0
0.2
0.4
0.5
0.6
0.8
1.0
Cu_3Al
$Cu_{2.5}Mn_{0.5}Al$
Cu_2MnAl
ATOMIC COMPOSITION $Cu_{3-x}Mn_xAl$
XBL7210-7116

Fig. 2

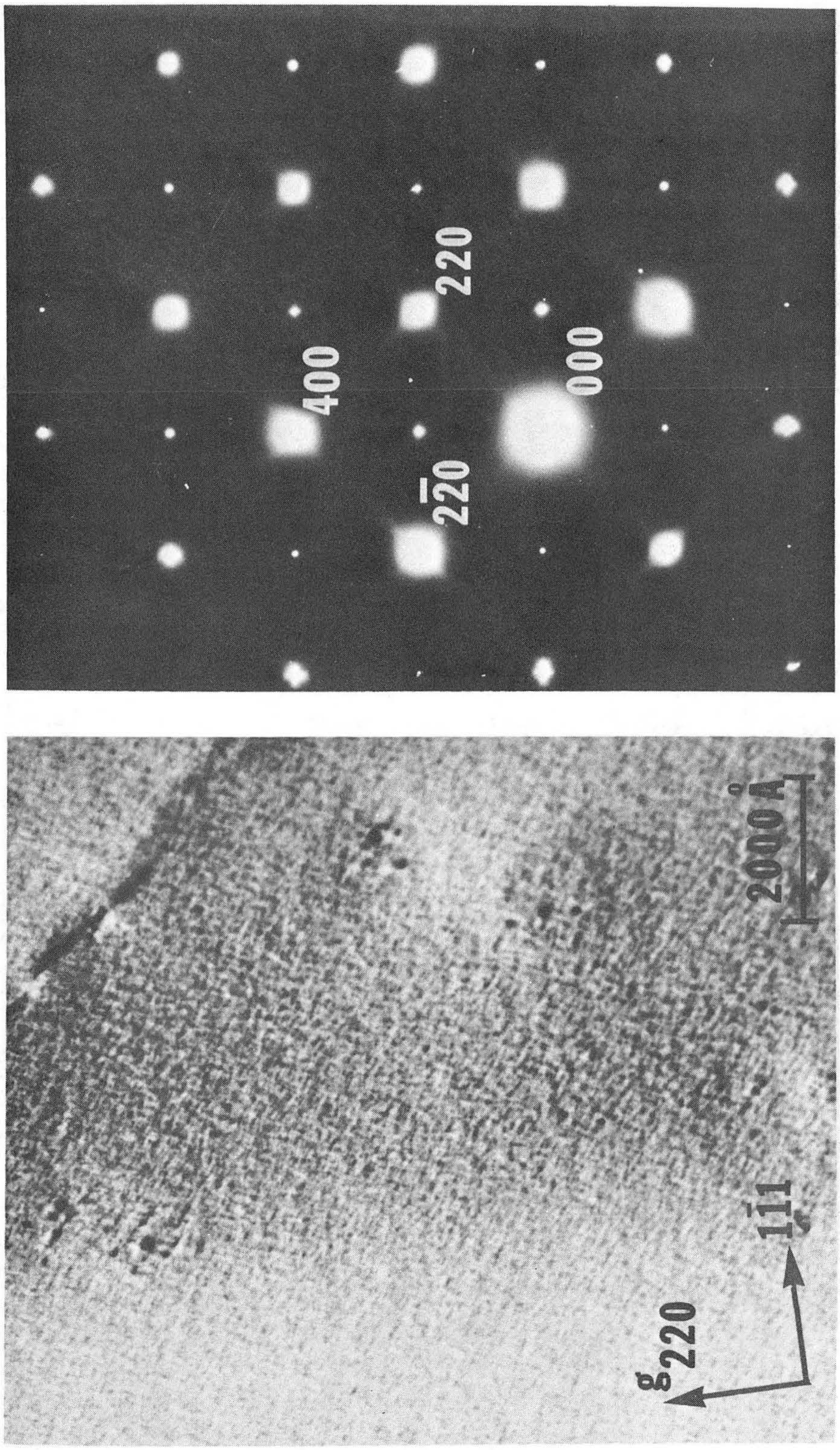

Fig. 3

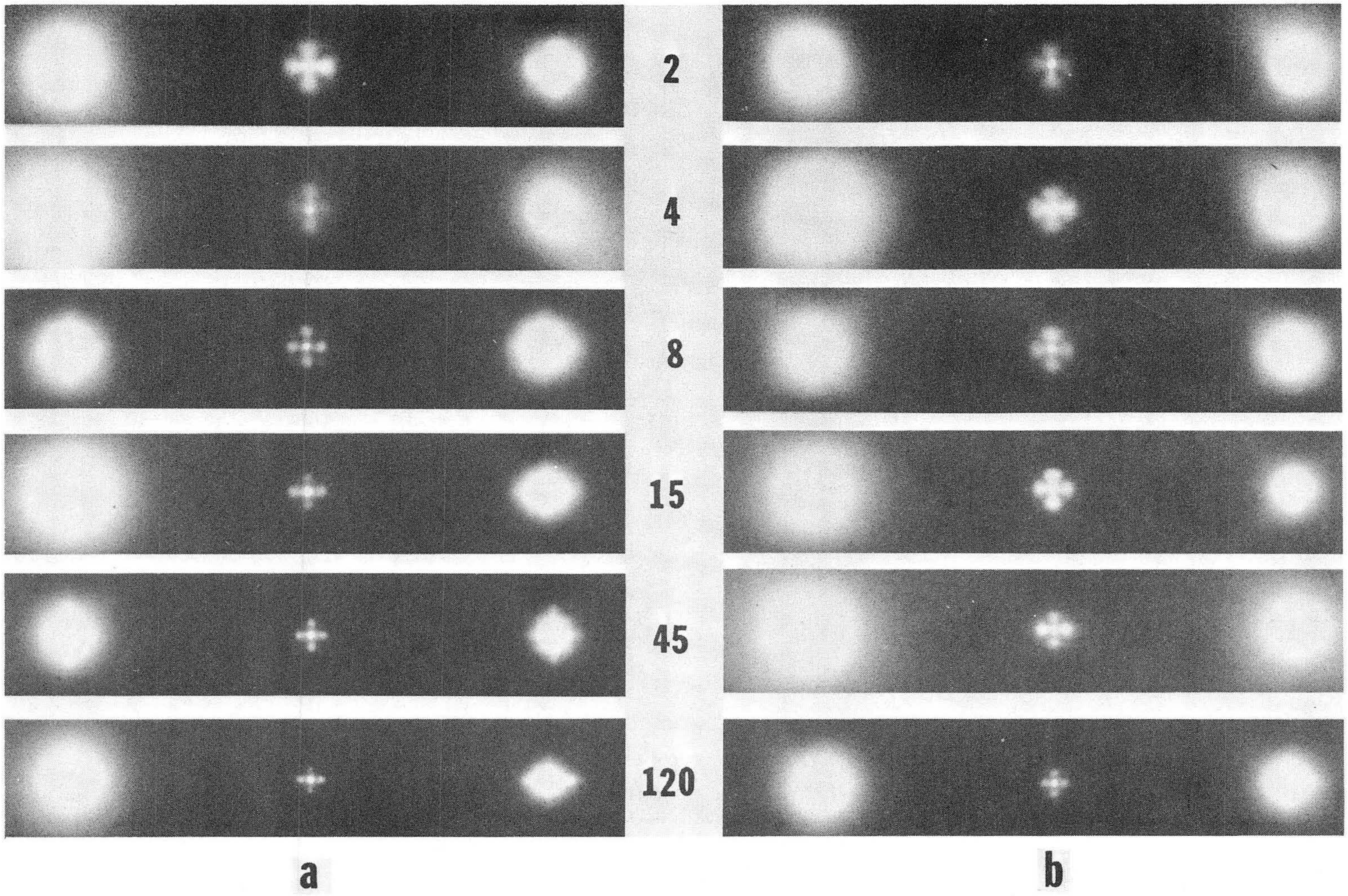

XBB 7210-5391

Fig. 4

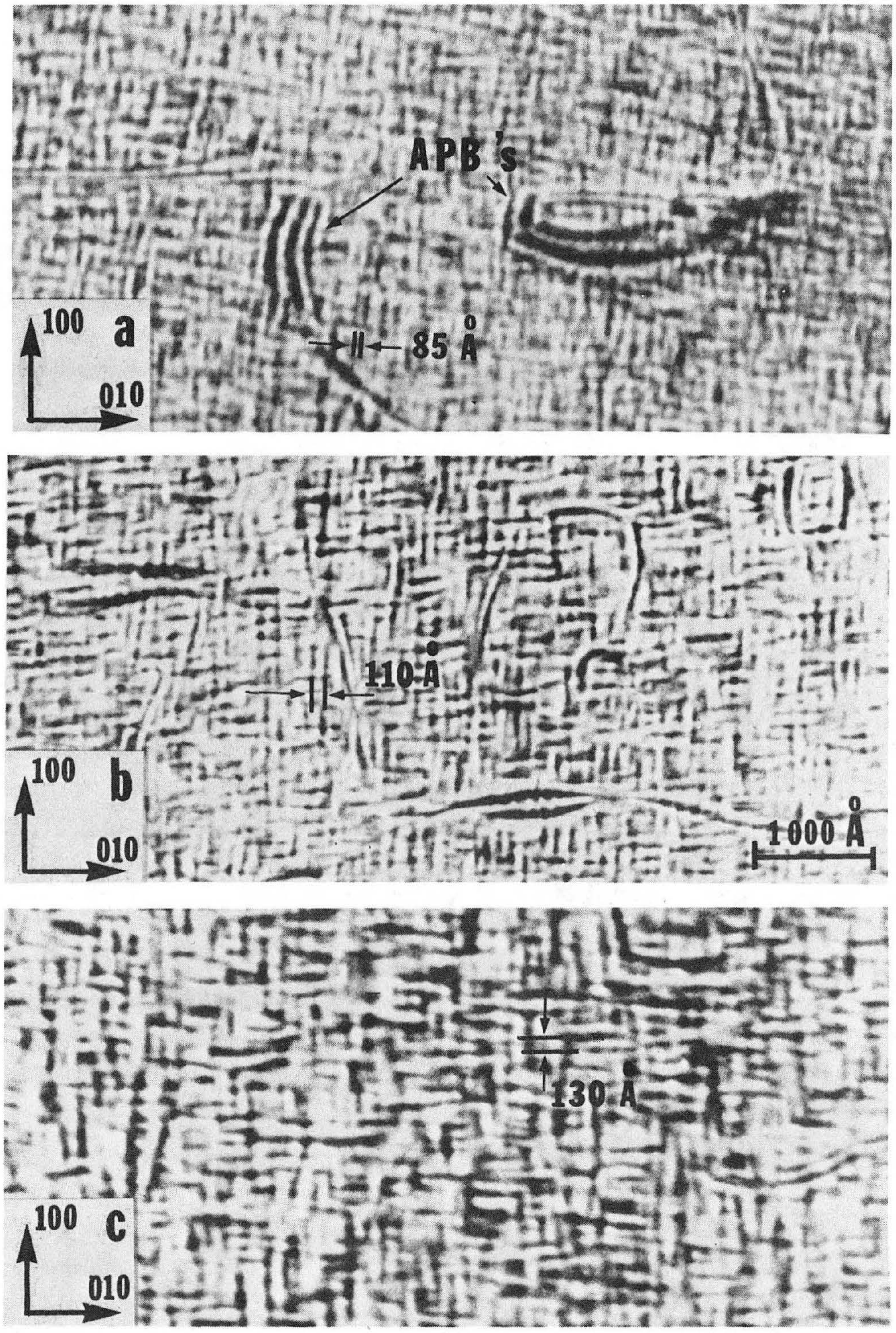

XBB 7210-5386

Fig. 5

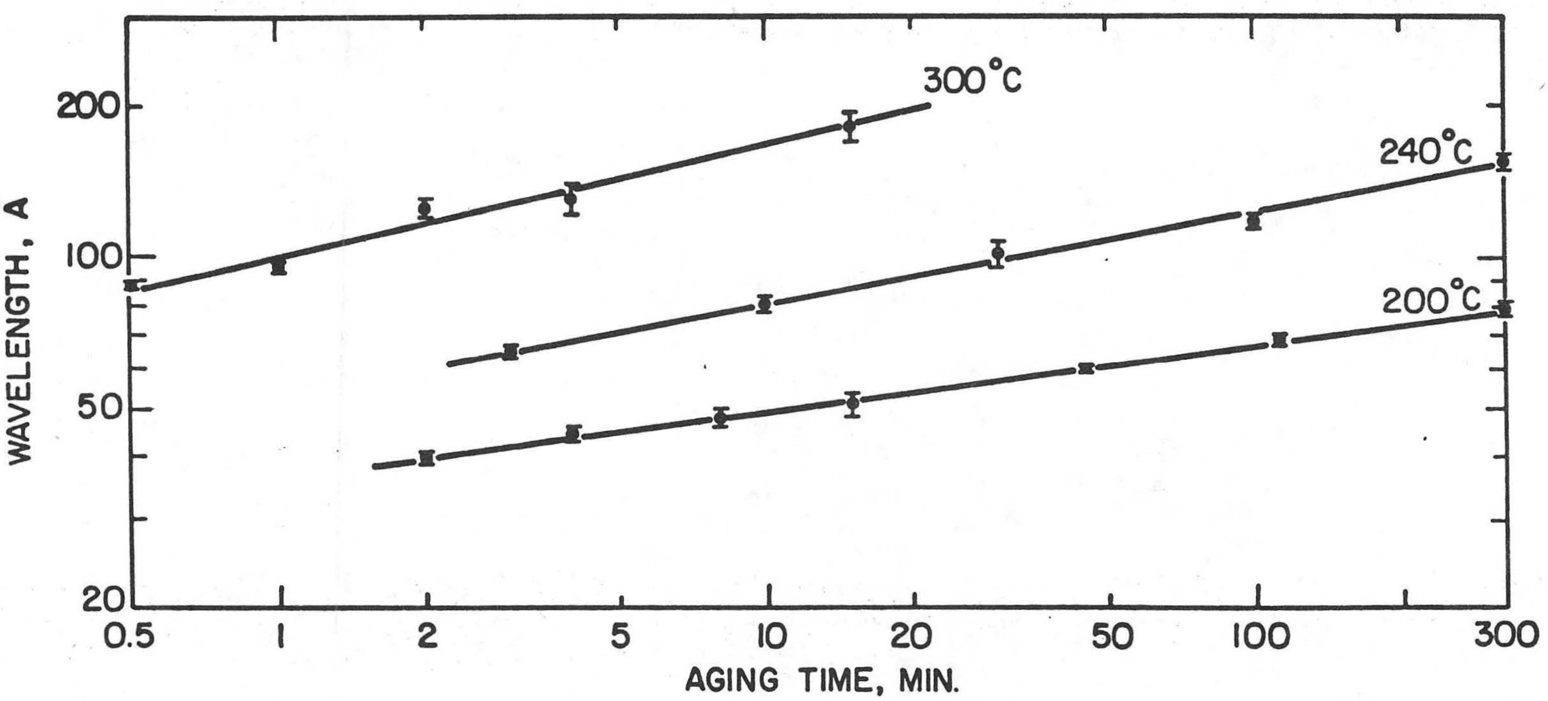

XBL7210-7115

Figg. 6

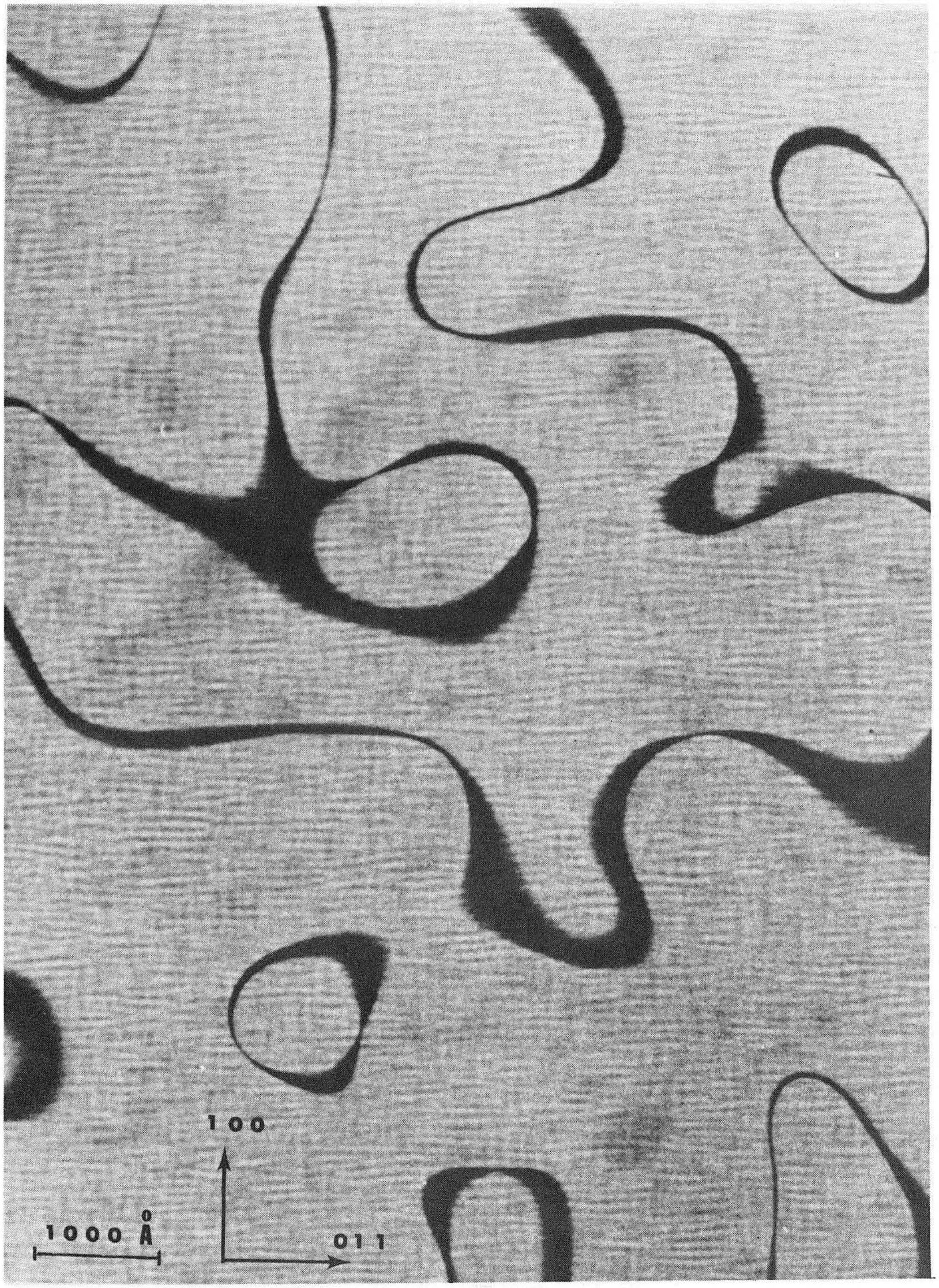

XBB 725-2682

Fig. 7

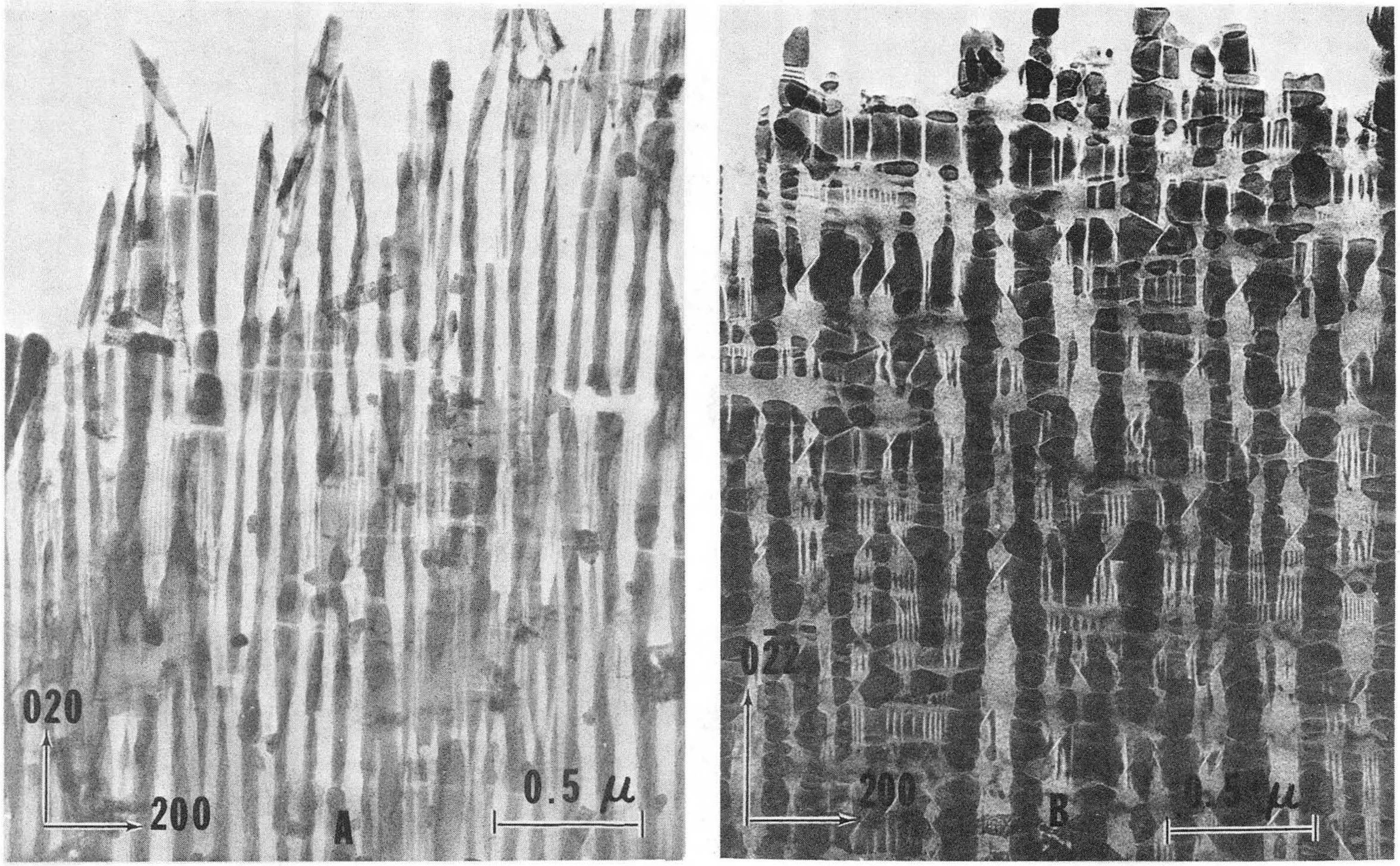

XBB 7210-5383

Fig. 8

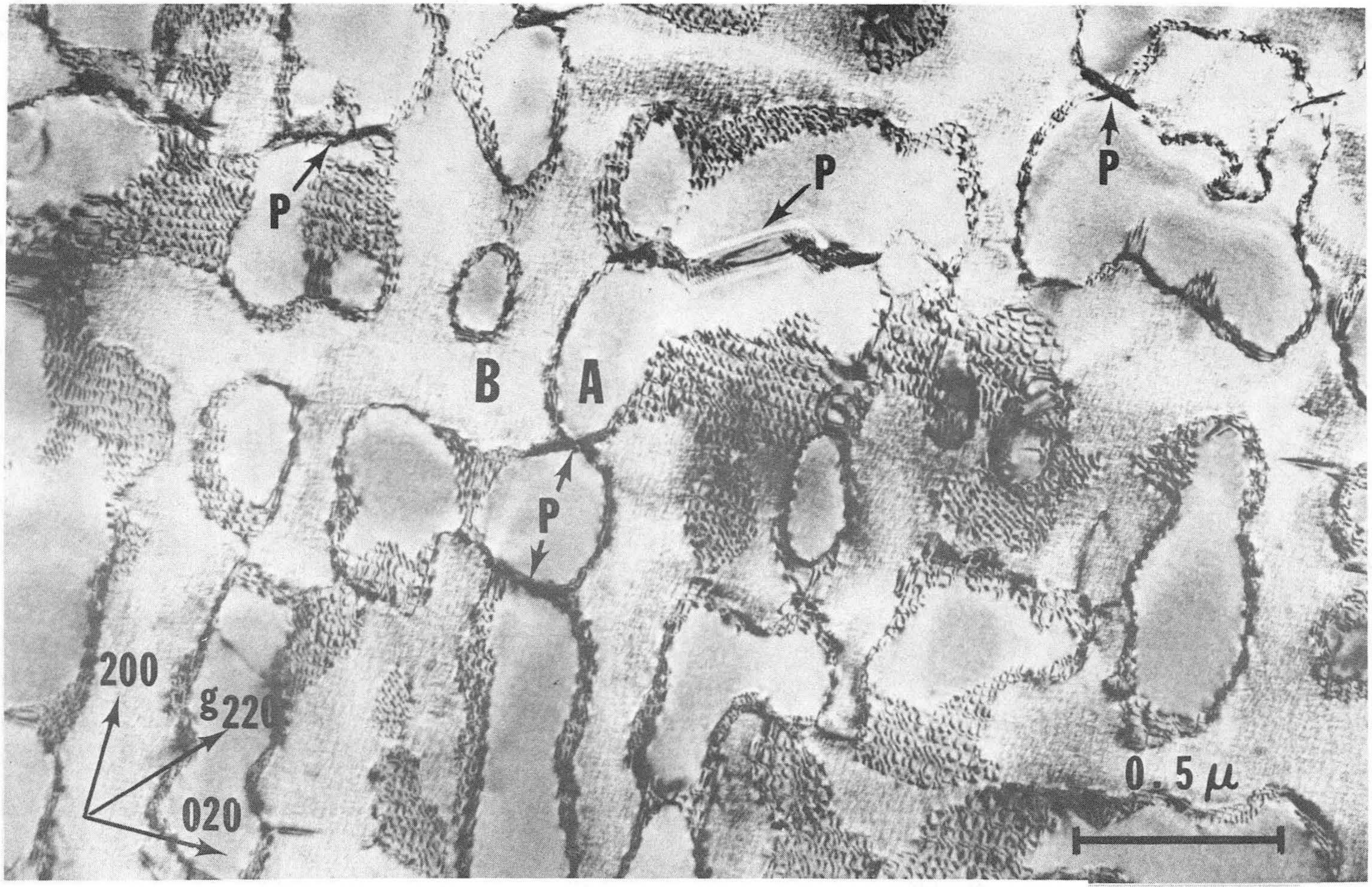

XBB 7211-5732

Fig. 9

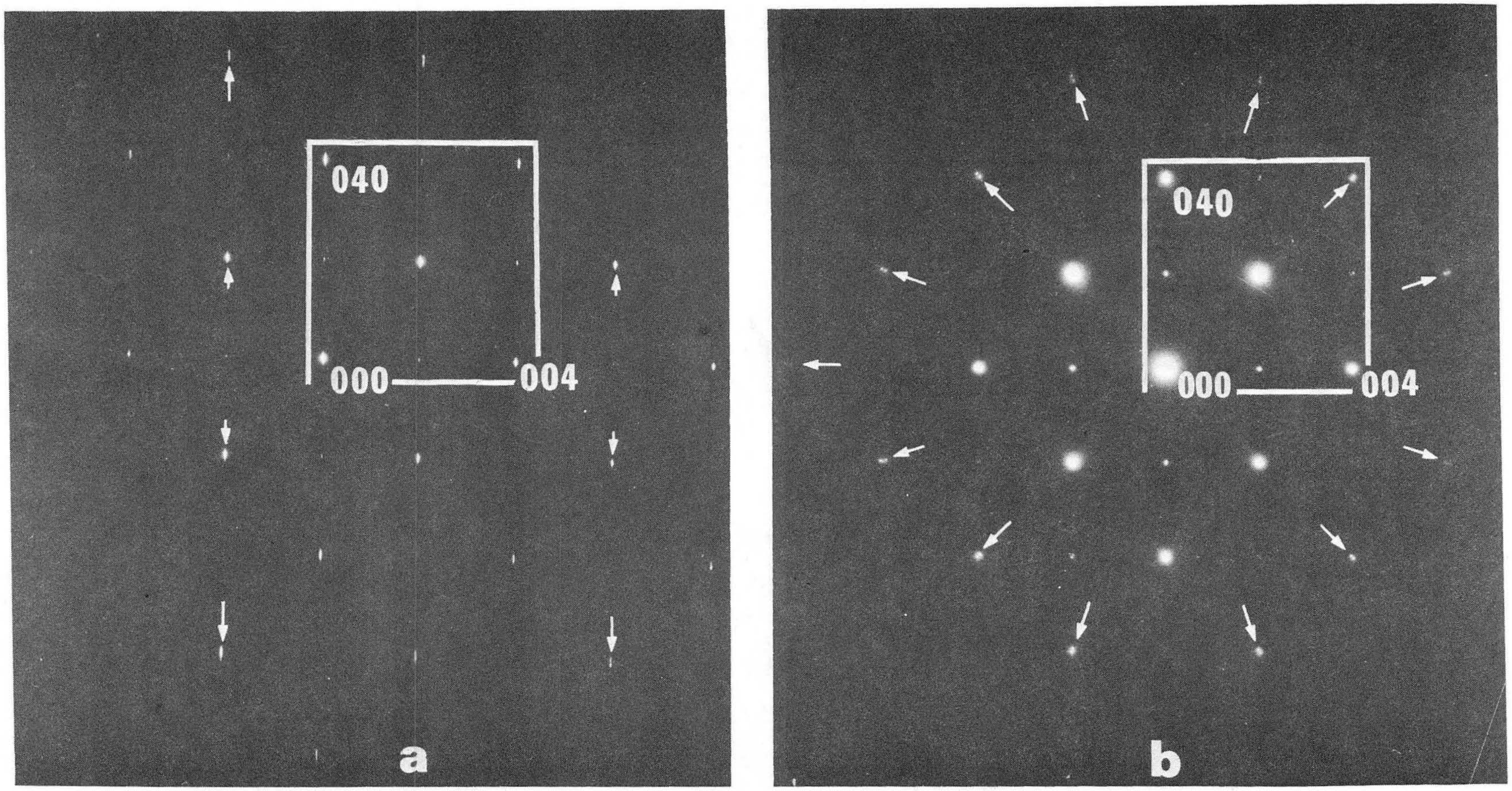

XBB 7210-5378

Fig. 10

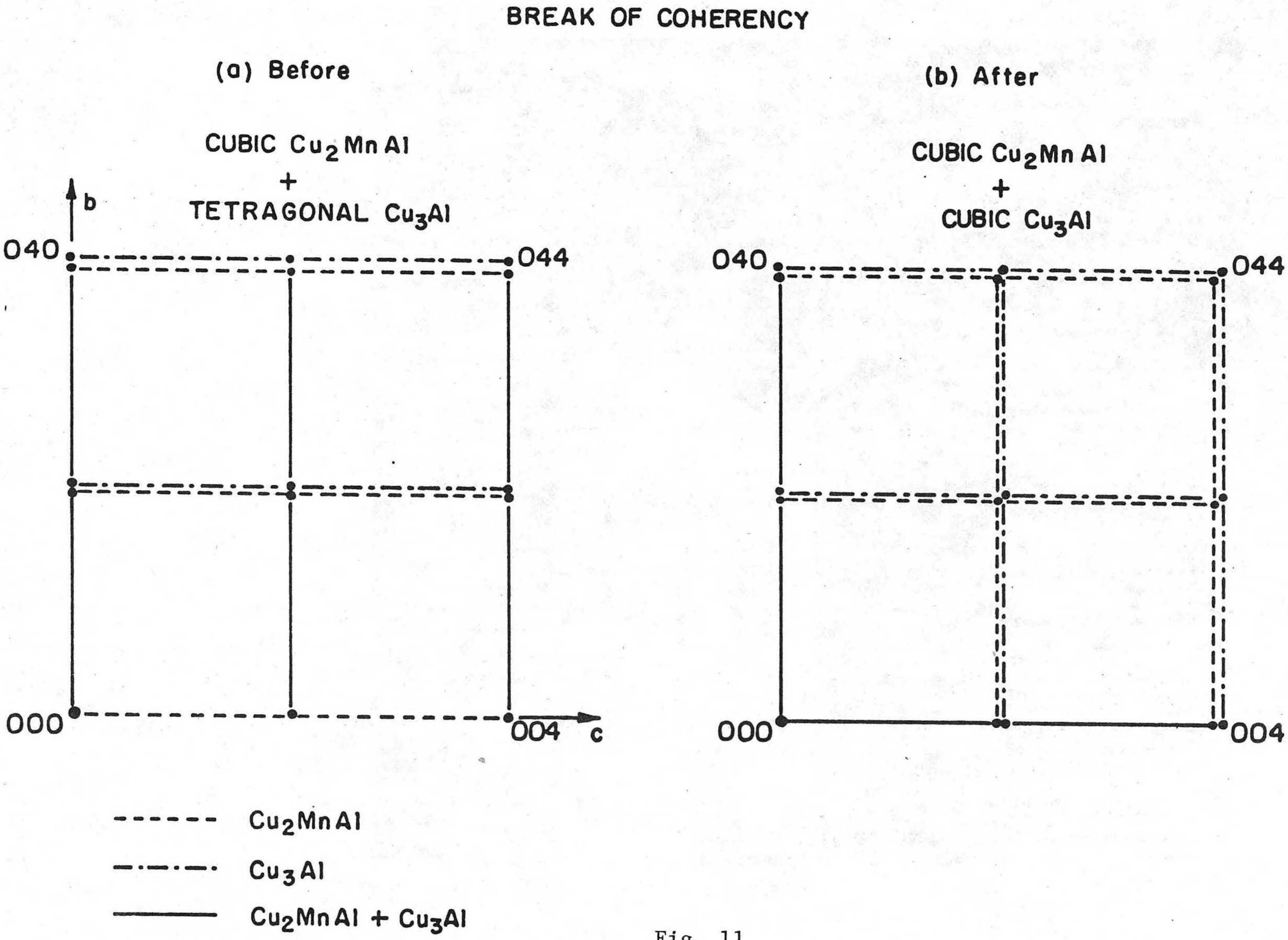

Fig. 11

XBL7210-7113

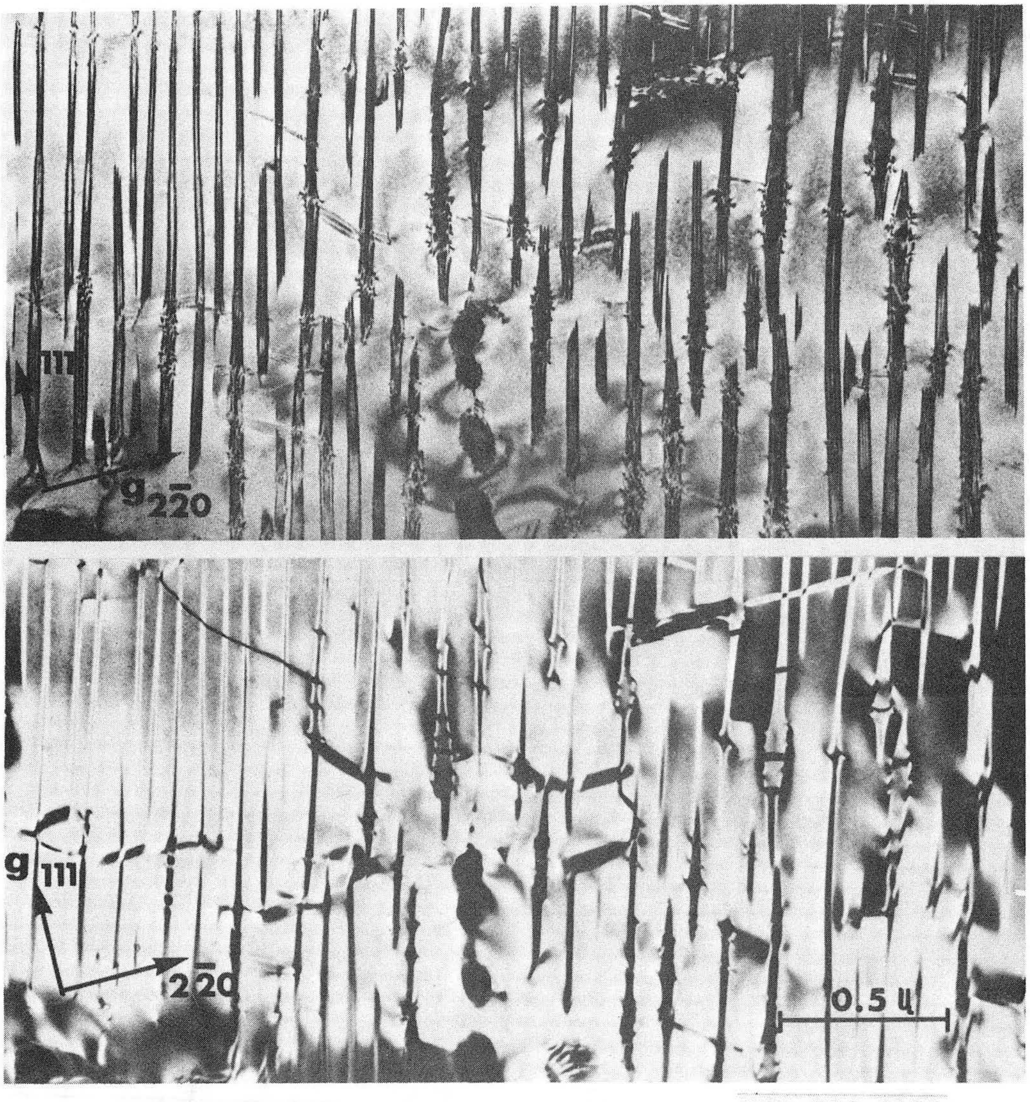

XBB 724-2180

Fig. 12

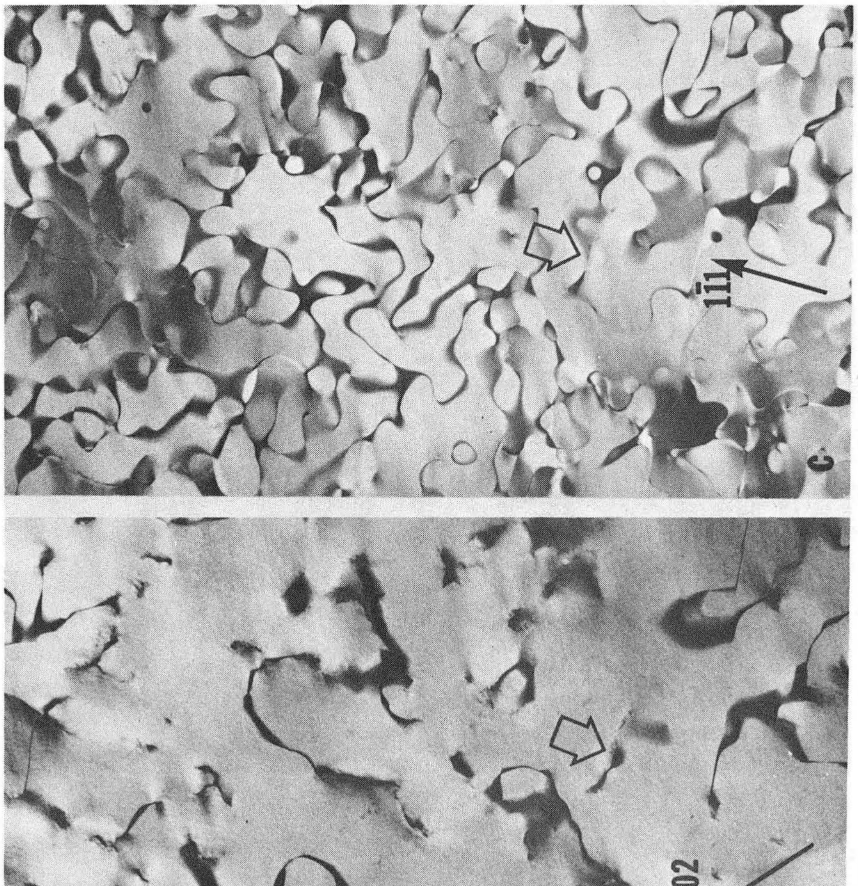

XBB 7210-5382

Fig. 13

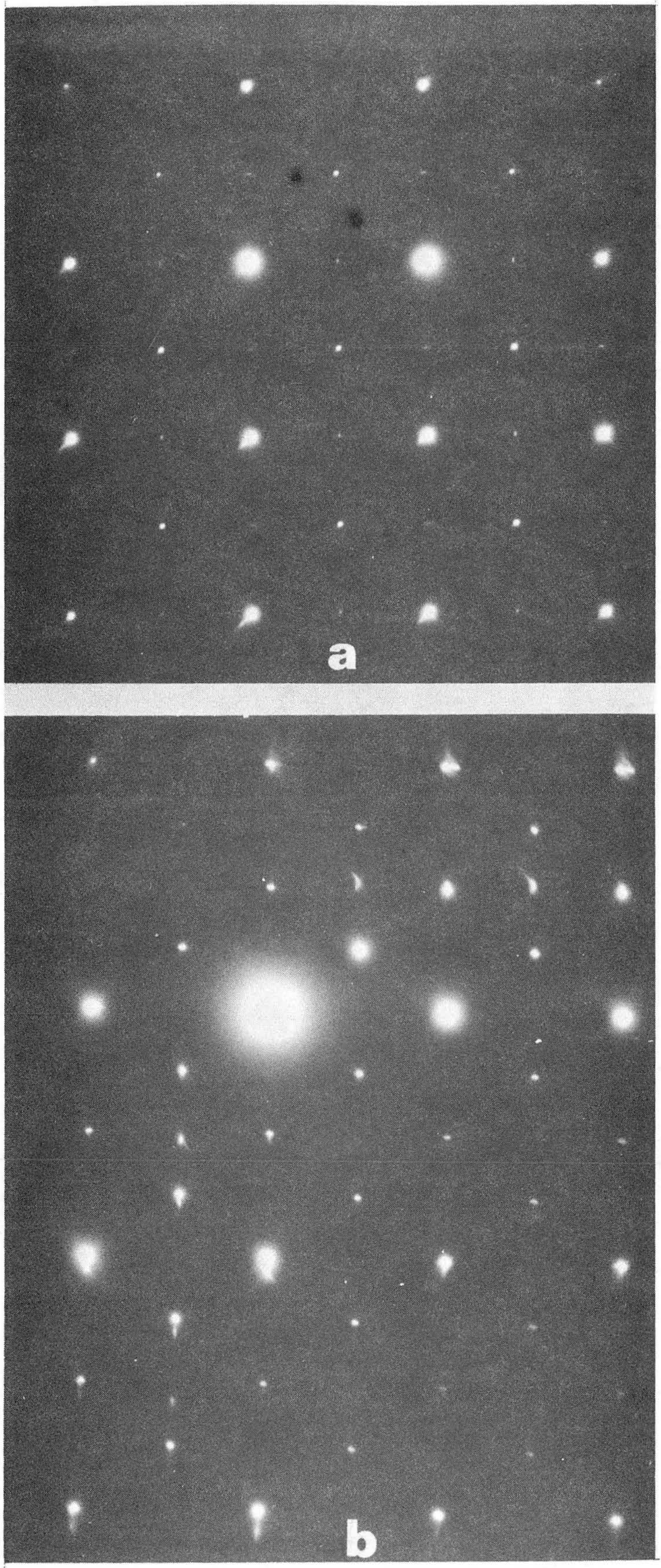

XBB 7211-5721

Fig. 14

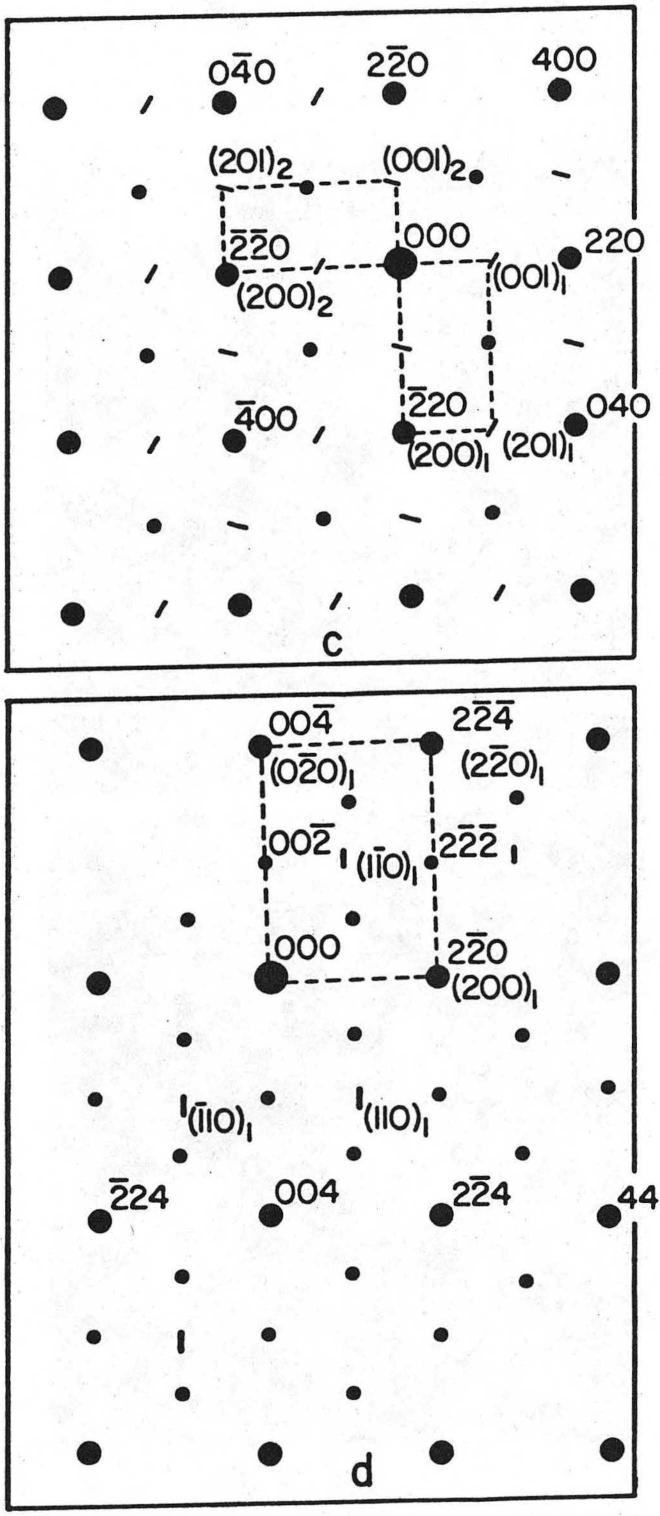

Fig. 14 (continued)

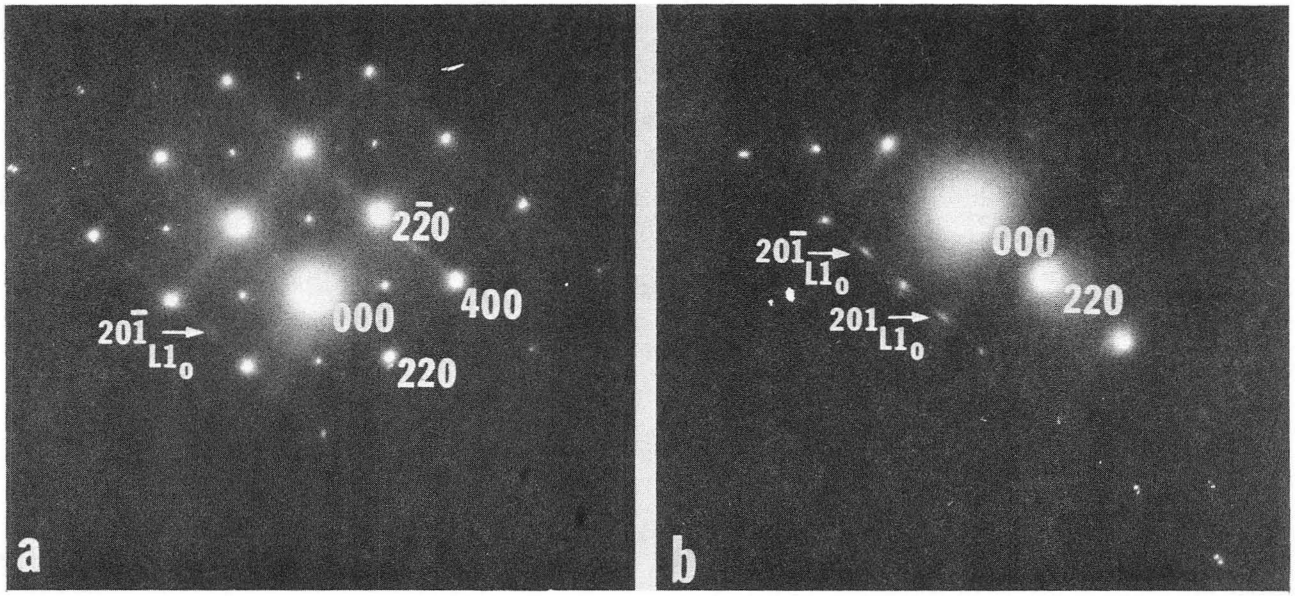

XBB 7211-5724

Fig. 15

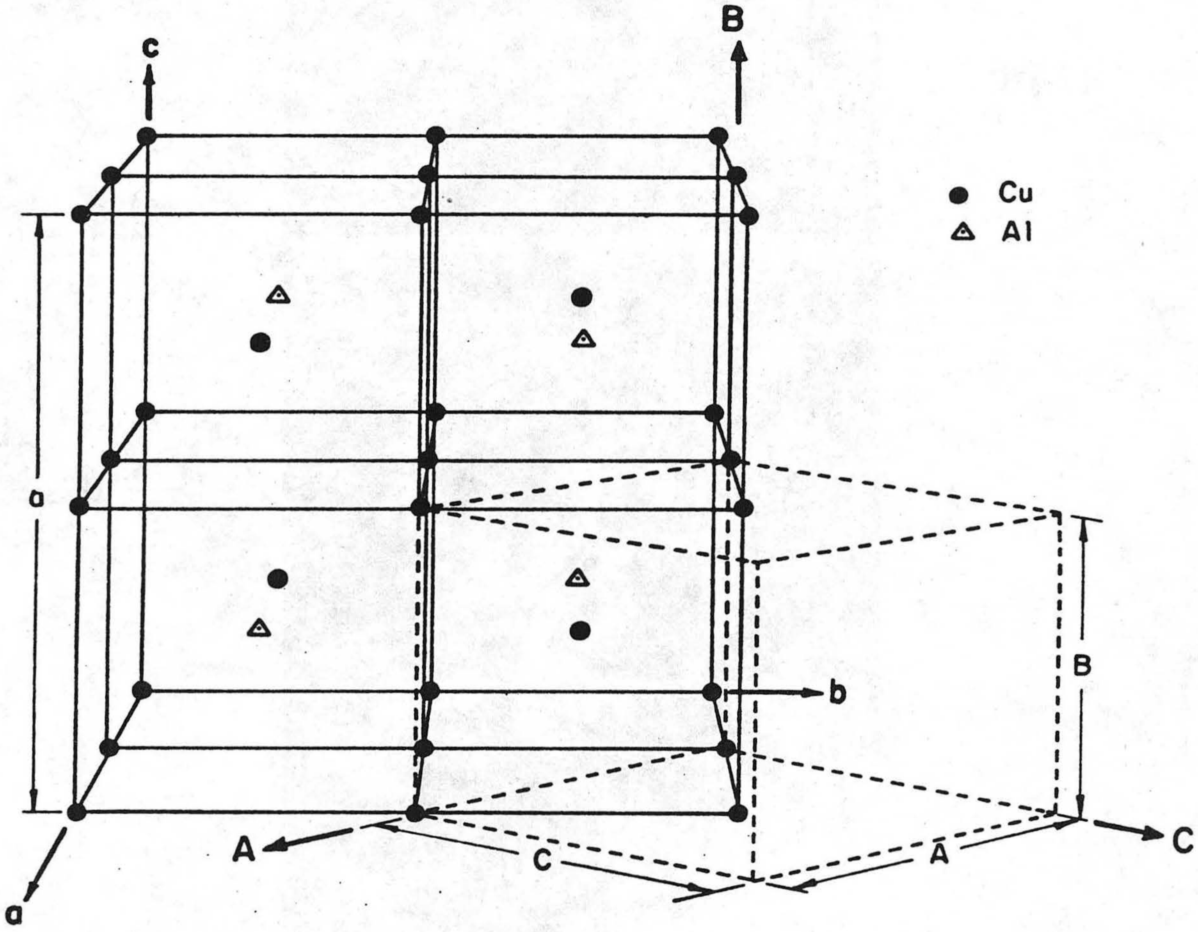

XBL7211-7259

Fig. 16

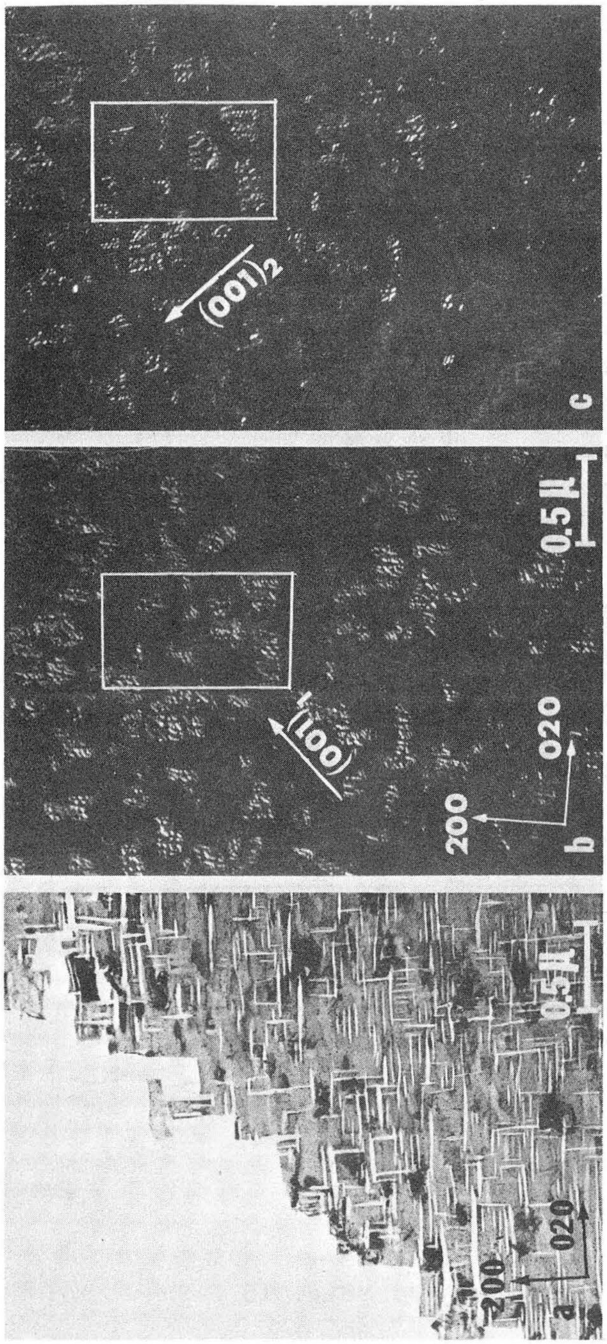

Fig. 17

XBB 7211-5723

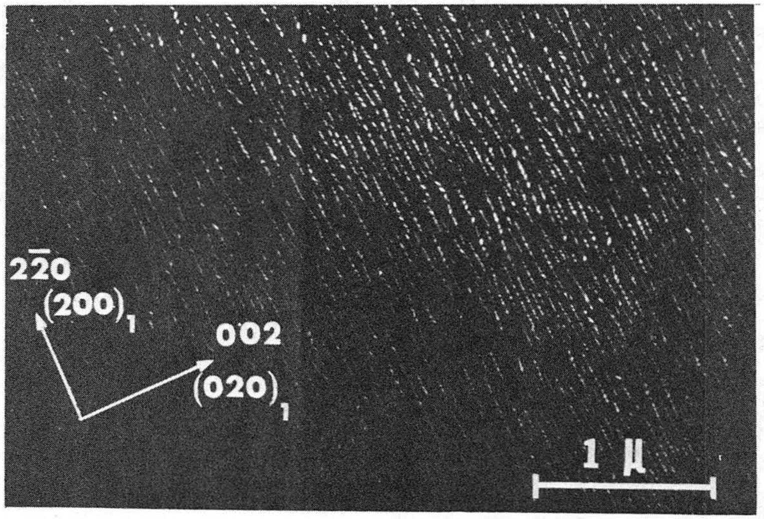

XBB 7211-5726

Fig. 18

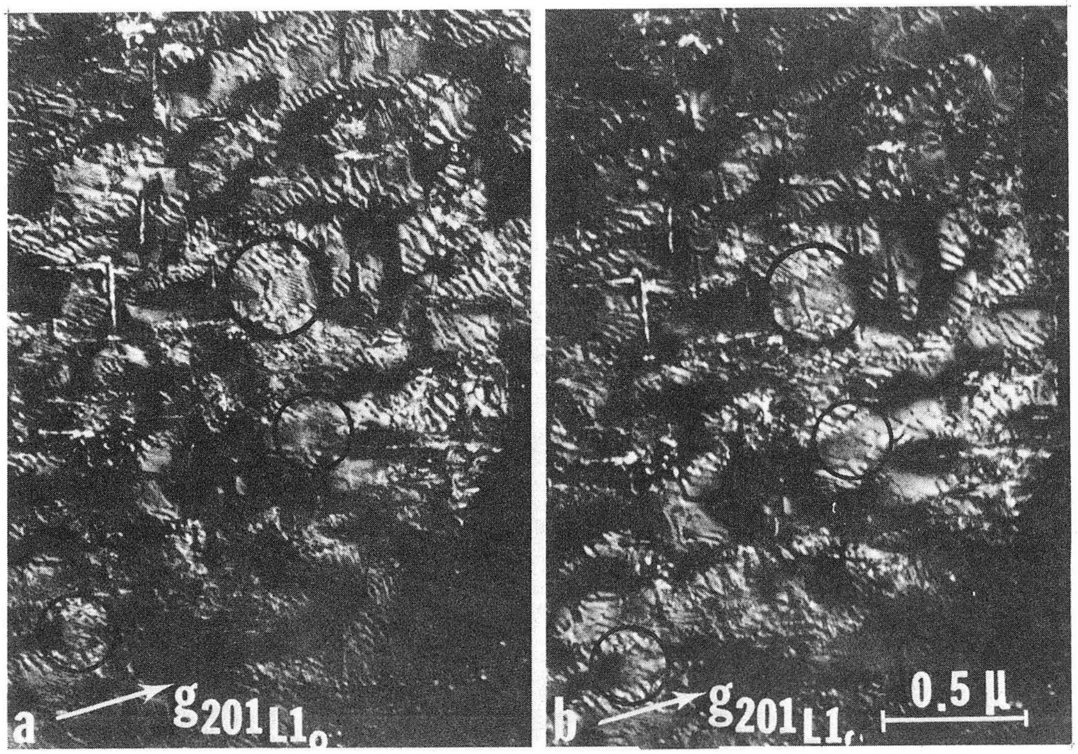

XBB 7211-5890

Fig. 19

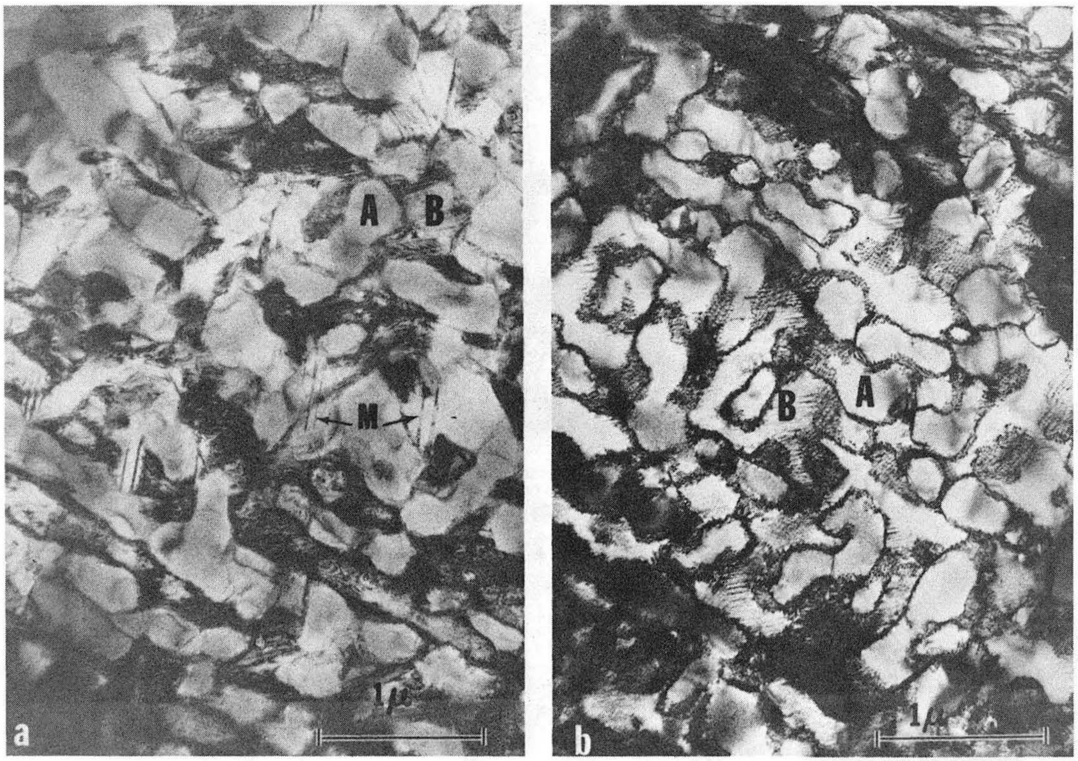

XBB 7211-5718

Fig. 20

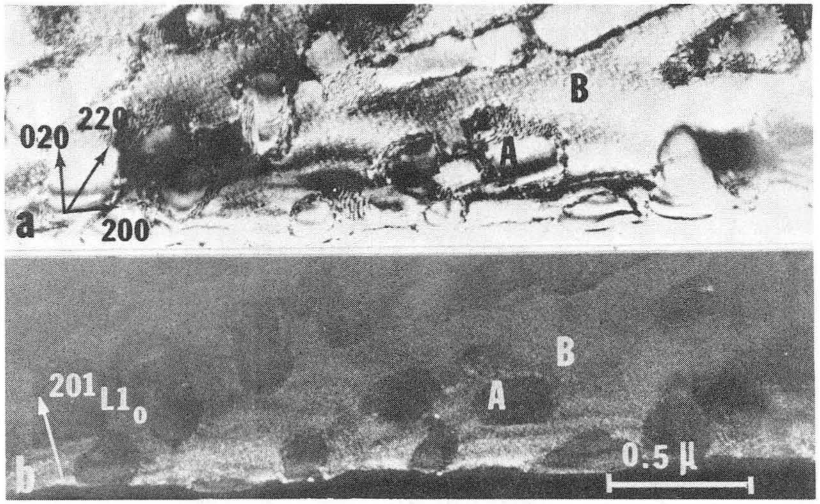

XBB 7211-5722

Fig. 21

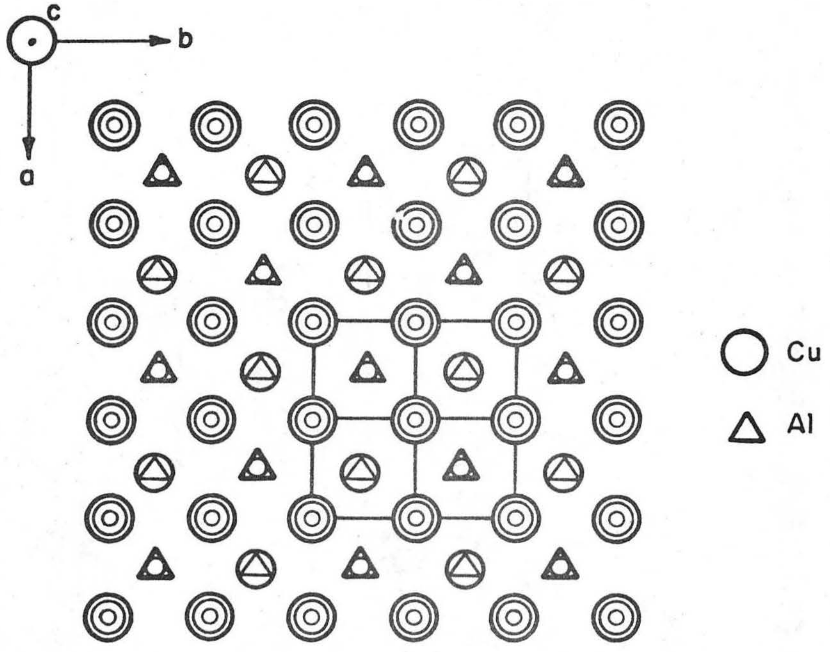

(a) DO_3 STRUCTURE

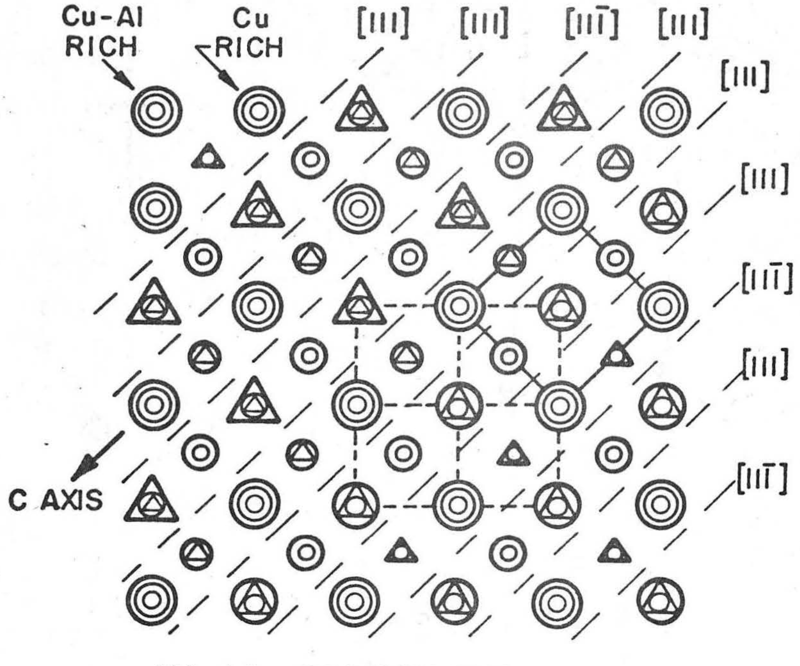

(b) $L1_0$ STRUCTURE

XBL7211-7265

Fig. 22

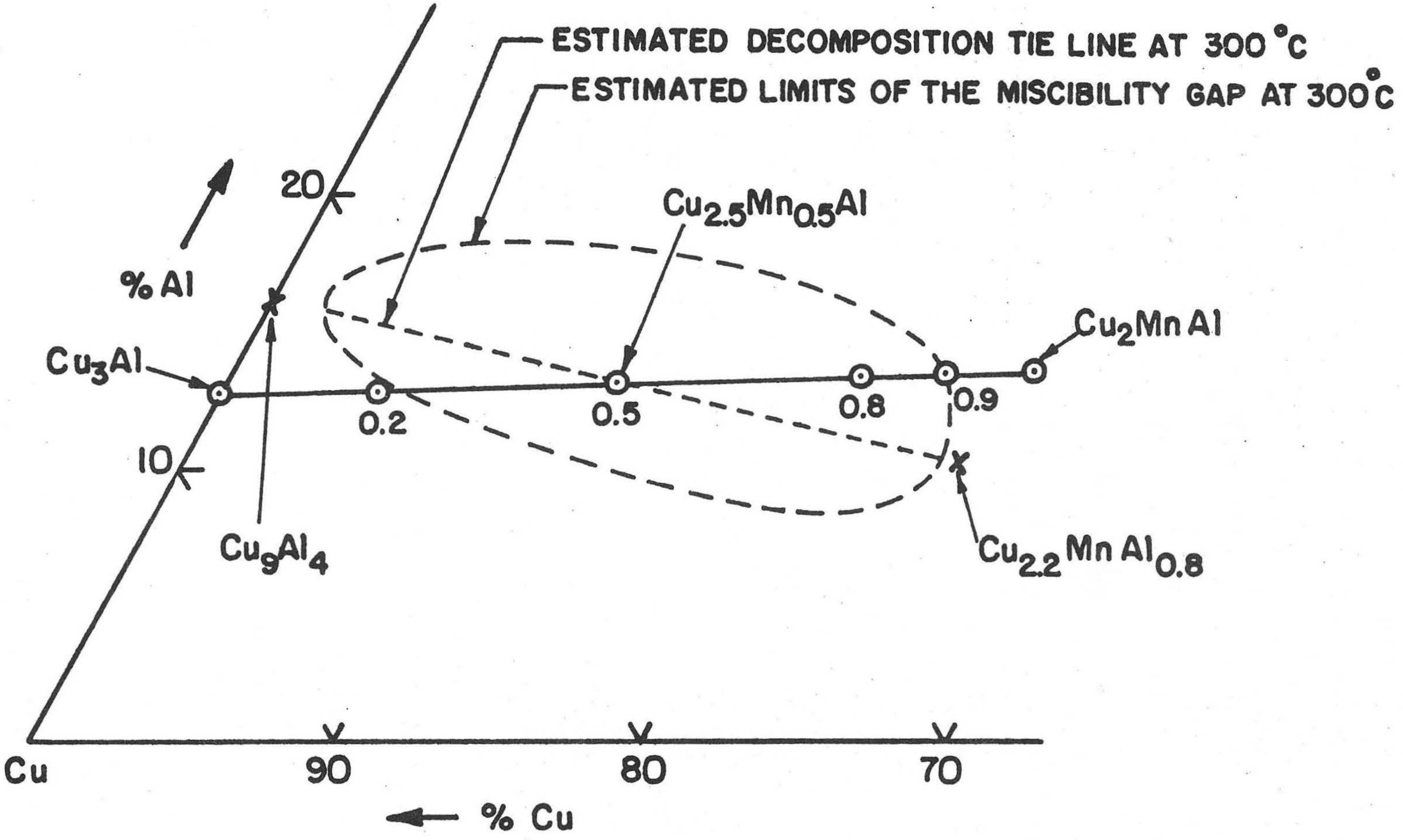

XBL7211-7263

Fig. 23

LEGAL NOTICE

This report was prepared as an account of work sponsored by the United States Government. Neither the United States nor the United States Energy Research and Development Administration, nor any of their employees, nor any of their contractors, subcontractors, or their employees, makes any warranty, express or implied, or assumes any legal liability or responsibility for the accuracy, completeness or usefulness of any information, apparatus, product or process disclosed, or represents that its use would not infringe privately owned rights.

TECHNICAL INFORMATION DIVISION
LAWRENCE BERKELEY LABORATORY
UNIVERSITY OF CALIFORNIA
BERKELEY, CALIFORNIA 94720